

Gauss-Bonnet Cosmology: large-temperature behaviour and bounds from Gravitational Waves

Anirban Biswas,^a Arpan Kar,^b Bum-Hoon Lee,^{b,c} Hocheol Lee,^{b,c} Wonwoo Lee,^b
Stefano Scopel,^{b,c} Liliana Velasco-Sevilla,^{b,c} Lu Yin^{d,e}

^a*Department of Physics & Lab of Dark Universe, Yonsei University, Seoul 03722, Republic of Korea*

^b*Center for Quantum Spacetime, Sogang University, Seoul 121-742, South Korea*

^c*Department of Physics, Sogang University, Seoul 121-742, South Korea*

^d*Department of Physics, Shanghai University, Shanghai 200444, China*

^e*Asia Pacific Center for Theoretical Physics (APCTP) San 31, Hyoja-dong, Nam-gu, Pohang 790-784, South Korea*

E-mail: anirban.biswas.sinp@gmail.com, arpankarphys@gmail.com,
bhl@sogang.ac.kr, insaying@sogang.ac.kr, warrrior@sogang.ac.kr,
scopel@sogang.ac.kr, liliana.velascosevilla@gmail.com,
lu.yin@apctp.org

ABSTRACT: We provide a transparent discussion of the high temperature asymptotic behaviour of Cosmology in a dilaton-Einstein-Gauss-Bonnet (dEGB) scenario of modified gravity with vanishing scalar potential. In particular, we show that it has a clear interpretation in terms of only three attractors (stable critical points) of a set of autonomous differential equations: $w = -\frac{1}{3}$, $w = 1$ and $1 < w < \frac{7}{3}$, where $w \equiv p/\rho$ is the equation of state, defined as the ratio of the total pressure and the total energy density. All the possible different high-temperature evolution histories of the model are exhausted by only eight paths in the flow of the set of the autonomous differential equations. Our discussion clearly explains why five out of them are characterized by a swift transition of the system toward the attractor, while the remaining three show a more convoluted evolution, where the system follows a meta-stable equation of state at intermediate temperatures before eventually jumping to the real attractor at higher temperatures. Compared to standard Cosmology, the regions of the dEGB parameter space with $w = -\frac{1}{3}$ show a strong enhancement of the expected Gravitational Wave stochastic background produced by the primordial plasma of relativistic particles of the Standard Model. This is due to the very peculiar fact that dEGB allows to have an epoch when the energy density ρ_{rad} of the relativistic plasma dominates the energy of the Universe while at the same time the rate of dilution with T of the total energy density is slower than what usually expected during radiation dominance. This allows to use the bound from Big Bang Nucleosynthesis (BBN) to put in dEGB a constraint $T_{\text{RH}} \lesssim (10^8 - 10^9)$ GeV on the reheating temperature of the Universe T_{RH} . Such BBN bound is complementary to late-time constraints from compact binary mergers.

Contents

1	Introduction	1
2	Summary of the dilaton- Einstein-Gauss-Bonnet scenario	3
3	Numerical solutions of the Friedmann equations	5
4	Asymptotic behaviours	9
4.1	Equivalent system of autonomous equations	9
4.2	Finite critical points	13
4.3	Critical points at infinity	17
4.4	Flows of the autonomous equation	18
5	Constraints from Gravitational Waves	21
5.1	GW stochastic background	21
5.1.1	Theoretical framework	21
5.1.2	Present and future stochastic GW observations	24
5.2	GW constraints from compact binary mergers	24
5.3	Summary of GW bounds	25
6	Conclusions	28
A	Thermal corrections	33

1 Introduction

In spite of its success in describing the observed Universe, General Relativity (GR) is believed to be incomplete, because it is difficult to reconcile with the other fundamental interactions of the Standard Model of Particle Physics (SM). Cosmology and astrophysics provide useful approaches to explore its possible extensions. In a previous paper [1], we analyzed a specific example of such extensions: the dilaton-Einstein-Gauss-Bonnet (dEGB) scenario, obtained by adding to the Einstein action a specific quadratic combination of the curvature non-minimally coupled to a scalar field [2, 3].

In extensions of Einstein Gravity such as string theory higher curvature terms are expected to appear and to become important in the early Universe. dEGB represents the simplest example with a higher curvature term of Horndeski’s theory, the most general scalar-tensor theory having equations of motion with second-order time derivatives in four-dimensional spacetime [4], in which the theory does not have a ghost state [5]. As a consequence, dEGB provides a very effective and popular framework to address both theoretical and phenomenological issues beyond General Relativity [6–16].

In Cosmology dEGB has been extensively studied during the inflationary era [2, 3, 17–27], in the reheating period at the end of inflation [28–31], and has been used to explain the accelerated expansion observed in the late-time Universe [32–36]. In Astrophysics dEGB has been used to study black holes with a scalar hair [37–48], and other objects [49–51]. The dEGB theory has been also tested against observed gravitational waves (GW) signals from black hole-black hole (BH-BH) or black hole-neutron star (BH-NS) merger events [52–56].

Specifically, in Ref. [1] we studied in detail the thermal evolution of a Cosmological model where GR is modified by the dEGB term and the potential of the scalar field vanishes. In particular, we focused on a range of temperatures between BBN and a few TeV, with the goal to constrain the specific scenario of the thermal decoupling of a Weakly Interacting Massive Particle (WIMP). Indeed, while we have no direct probe of its Universe expansion rate, the epoch between reheating and Big Bang Nucleosynthesis is crucial to shed light on physics beyond the SM such as the nature of Dark Matter [57–64] or the origin of the baryon asymmetry in the Universe [65, 66].

Interestingly, the numerical analysis of Ref. [1] unveiled that, in spite of a high degree of non linearity and phenomenological complexity at low temperatures, at large-enough temperatures dEGB exhibits instead only very few asymptotic behaviours, characterized by the equation of state $w = p/\rho$ (where ρ and p are the total energy density and the pressure of the Universe, respectively), when the model is required to reproduce Standard Cosmology at BBN. Specifically, the study of Ref. [1] showed that within dEGB the asymptotic value at high temperature of the equation of state falls only into three cases: $w = 1$, $w = -1/3$, $1 \leq w \lesssim 2.3$. Clearly, such behaviour suggests a pattern of attractor solutions emerging at high temperatures. However, the numerical approach that we used in Ref. [1] to solve the coupled Friedmann differential equations of the system did not provide a transparent interpretation of such pattern, that also required to extend the analysis beyond the temperature relevant for the WIMP decoupling effect that we wished to discuss. As a consequence, in Ref. [1] we did not attempt to provide a systematic discussion of the asymptotic behaviour of dEGB at high temperatures. The goal of the present paper is to fill this gap, extending the analysis of dEGB to higher temperatures and providing a transparent and systematic discussion of its high temperature asymptotic behaviour. The main result of the present analysis is twofold:

- An appropriate change of variables [18] allows to express the evolution of the dEGB Friedmann equations in terms of a set of two autonomous coupled differential equations whose critical points and attractors can be studied in a straightforward way, providing a clear and transparent understanding of the pattern of the high-temperature asymptotic behaviours that emerged from the numerical analysis of Ref. [1]. In particular, such interpretation allows also to understand that one of the regimes identified as asymptotic in Ref. [1] was indeed meta-stable, i.e. would eventually converge to one of the other possible asymptotic regimes at higher temperatures (such feature was irrelevant for the WIMP analysis of Ref. [1]).
- In the regions of the dEGB parameter space where the asymptotic behaviour of the equation of state is $w = -1/3$ the potential signal of stochastic GW produced by

the thermal plasma of the Standard Model particles in the early Universe [67, 68] can exceed the Big Bang Nucleosynthesis (BBN) bounds for values of the reheating temperature as low as $T_{RH} \simeq 10^9$ GeV. This is at variance with Standard Cosmology, where for T_{RH} as high as 10^{16} GeV such contribution is diluted away and negligible at the time of BBN, and provides some prospects to detect such signal experimentally in future detectors sensitive to the high-frequency GW spectrum [69, 70].

Our paper is organized as follows. In Section 2 we outline the dEGB scenario of modified gravity and fix our notations; in Section 3 we extend to $T \lesssim 10^{16}$ GeV the discussion of the numerical solutions of the Friedmann equations in dEGB Cosmology of Ref. [1]; in Section 4 we re-express the Friedmann equations discussed in Section 3 in terms of a system of two coupled autonomous differential equations and provide a detailed discussion of its critical points and attractors that allows to interpret the numerical results of Section 3 in a transparent way (in particular such discussion is summarized schematically in Figure 8 and in Table 1). Section 5 is devoted to the GW bounds, with Section 5.1 dealing with the stochastic background and Section 5.2 with Late Universe constraints from BH-BH and BH-NS merger events. In particular, in Section 5.1.1 we summarize how the GW stochastic signal is calculated, and in Section 5.1.2 we discuss its possible observable implications. Finally, we combine the observational constraints on dEGB Cosmology from GW observables in Section 5.3, and provide our Conclusions in Section 6. For completeness, in Appendix A we summarize the thermal corrections calculated in Ref. [68] that are used in Section 5.1.1 to calculate the source term of the stochastic GW background.

2 Summary of the dilaton- Einstein-Gauss-Bonnet scenario

In order to fix our notation, in this Section we briefly outline the dEGB scenario that we analyzed in [1]. More details can also be found in [1, 18, 37]. The action is given by

$$S = \int_{\mathcal{M}} \sqrt{-g} d^4x \left[\frac{R}{2\kappa} - \frac{1}{2} \nabla_\mu \phi \nabla^\mu \phi - V(\phi) + f(\phi) R_{\text{GB}}^2 + \mathcal{L}_m^{\text{rad}} \right], \quad (2.1)$$

where $\kappa \equiv 8\pi G = 1/M_{\text{PL}}^2$ (where M_{PL} is the reduced Planck mass), R is the Ricci scalar of the spacetime \mathcal{M} , $R_{\text{GB}}^2 = R^2 - 4R_{\mu\nu}R^{\mu\nu} + R_{\mu\nu\rho\sigma}R^{\mu\nu\rho\sigma}$ is the Gauss-Bonnet term and $\mathcal{L}_m^{\text{rad}}$ describes radiation (i.e. all the relativistic species). Following the same approach that we adopted in Ref. [1] we will assume $V = 0$. The function $f(\phi)$ is a coupling function between the scalar field and the Gauss-Bonnet term for which we assume

$$f(\phi) = \alpha e^{\gamma\phi}, \quad (2.2)$$

where α and γ are constants. An exponential form for f arises naturally within theories where gravity is coupled to the dilaton [37]. In particular, although in string theory the natural sign of the α coefficient is positive [6], in Refs. [18, 45, 46] it was shown that for both signs of α black-hole solutions can be found. In our phenomenological analysis we will adopt both signs.

By varying the action the equation of motion for the scalar field $\square\phi + f'R_{\text{GB}}^2 = 0$, and Einstein's equations $R_{\mu\nu} - \frac{1}{2}g_{\mu\nu}R = \kappa T_{\mu\nu}^{\text{tot}}$ can be obtained, where $T_{\mu\nu}^{\text{tot}} = T_{\mu\nu}^{\phi} + T_{\mu\nu}^{\text{GB}} + T_{\mu\nu}^{\text{rad}}$ is given by three contributions, corresponding to the scalar field, the GB term and radiation. In particular, $T_{\mu\nu}^{\text{tot}}$ satisfies the continuity equation, although due to the interaction between the Gauss-Bonnet term and the scalar field the two components $T_{\mu\nu}^{\phi}$ and $T_{\mu\nu}^{\text{GB}}$ do not satisfy it separately.

The evolution of the universe is well described by homogeneous and isotropic space on a large scale. We take the spatially flat Friedmann-Lemaître-Robertson-Walker (FLRW) metric, i.e.,

$$ds^2 = -dt^2 + a^2(t)\delta_{ij}dx^i dx^j, \quad (2.3)$$

in terms of the scale factor $a(t)$. As a consequence, the scalar field depends only on time, $\phi = \phi(t)$. From the energy-momentum tensor one can then obtain the contributions ρ_i and p_i to the energy density and the pressure, with $i = \phi, \text{GB}, \text{rad}$. They enter the Friedmann equations in the familiar form:

$$H^2 = \frac{\kappa}{3}\rho, \quad (2.4)$$

$$\dot{H} = -\frac{\kappa}{2}(\rho + p), \quad (2.5)$$

$$\ddot{\phi} + 3H\dot{\phi} + V'_{\text{GB}} = 0, \quad (2.6)$$

where $\rho = \rho_{\phi} + \rho_{\text{GB}} + \rho_{\text{rad}}$, $p = p_{\phi} + p_{\text{GB}} + p_{\text{rad}}$, and, each component has the following explicit form:

$$\rho_{\phi} = p_{\phi} = \frac{1}{2}\dot{\phi}^2, \quad (2.7)$$

$$\rho_{\text{GB}} = -24\dot{f}H^3 = -24f'\dot{\phi}H^3 = -24\alpha\gamma e^{\gamma\phi}\dot{\phi}H^3, \quad (2.8)$$

$$\begin{aligned} p_{\text{GB}} &= 8\left(f''\dot{\phi}^2 + f'\ddot{\phi}\right)H^2 + 16f'\dot{\phi}H(\dot{H} + H^2) \\ &= 8\frac{d(\dot{f}H^2)}{dt} + 16\dot{f}H^3 = 8\frac{d(\dot{f}H^2)}{dt} - \frac{2}{3}\rho_{\text{GB}}, \end{aligned} \quad (2.9)$$

$$\rho_{\text{rad}} = 3p_{\text{rad}} = \frac{\pi^2}{30}g_*T^4, \quad (2.10)$$

where g_* is the number of effective relativistic degrees of freedom in equilibrium with the thermal bath. Notice that, as far as the evolution of the Hubble constant H is concerned, in Eqs. (2.4) and (2.5) ρ and p can be interpreted as the total energy density and the pressure of the Universe with ρ positive-defined. On the other hand, ρ_{GB} and p_{GB} in Eqs. (2.8) and (2.9), which can be interpreted as the effective energy density and pressure coming from the GB term, are not necessarily positive. Moreover, in Eq. (2.6) V'_{GB} is

$$V'_{\text{GB}} \equiv -f'R_{\text{GB}}^2 = -24f'H^2(\dot{H} + H^2) = 24\alpha\gamma e^{\gamma\phi}qH^4, \quad (2.11)$$

which is technically not the gradient of a potential, but just an excess of notation to indicate that it drives the scalar field evolution. In Eq.(2.11) $q = -\frac{\ddot{a}a}{\dot{a}^2} = \frac{1}{2}(1 + 3w)$ is the usual deceleration parameter.

3 Numerical solutions of the Friedmann equations

In this Section, we solve Eqs.(2.5) and (2.6) numerically, after writing them as a set of three first order coupled differential equations, with the goal to investigate their high-temperature behaviour. Throughout the paper we present our numerical results in geometric units defined by $\kappa = 8\pi G = 1$, $c = 1$ ¹.

Assuming iso-entropic expansion ($sa^3 = \text{constant}$ with $s = (2\pi^2/45)g_{*s}T^3$ the entropy density and $g_{*s}(T)$, the number of entropy degrees of freedom), the change of variable from time to temperature is given as usual as

$$\frac{dT}{dt} = -\frac{HT}{\beta}, \quad (3.1)$$

where

$$\beta = \left(1 + \frac{1}{3} \frac{d \ln g_{*s}}{d \ln T}\right), \quad (3.2)$$

and before neutrino decoupling $g_{*s} = g_*$ [71]. We fix the boundary conditions at the temperature of Big Bang Nucleosynthesis, $T_{\text{BBN}} = 1$ MeV, by setting $\phi(T_{\text{BBN}}) \equiv \phi_{\text{BBN}}$, $\dot{\phi}(T_{\text{BBN}}) \equiv \dot{\phi}_{\text{BBN}}$ and $H(T_{\text{BBN}}) \equiv H_{\text{BBN}}$ and evolve the differential equations “backward in time” to higher temperatures. Since the solutions of the Friedmann equations become invariant under a simultaneous change of sign of ϕ_{BBN} , $\dot{\phi}_{\text{BBN}}$ and γ , without loss of generality in our analysis we fix $\dot{\phi}(T_{\text{BBN}}) > 0$ and study both signs of γ . We stop our integration at $T \simeq 10^{16}$ GeV, since we assume that the thermal plasma is kept in thermal equilibrium by standard perturbative interactions, which are frozen out and are ineffective at higher temperatures [72].

As far as the boundary condition for ϕ is concerned, we note that a shift of ϕ_{BBN} is equivalent to a redefinition of the α parameter

$$\phi'_{\text{BBN}} = \phi_{\text{BBN}} + \phi_0, \quad \alpha' = \alpha e^{-\gamma\phi_0}, \quad \gamma' = \gamma. \quad (3.3)$$

In other words, any choice of ϕ_{BBN} corresponds to a specific gauge fixing and the quantity

$$\tilde{\alpha} = \alpha e^{\gamma\phi_{\text{BBN}}}, \quad (3.4)$$

is invariant under the gauge transformation (3.3). In our analysis, we will show our results in terms of $\tilde{\alpha}$ (which is equivalent to adopt the gauge $\phi_{\text{BBN}} = 0$)².

The ratio of $\rho_\phi(T_{\text{BBN}}) = \frac{1}{2}\dot{\phi}_{\text{BBN}}^2$ to the total energy density at BBN, $\eta = \frac{\rho_\phi(T_{\text{BBN}})}{\rho(T_{\text{BBN}})}$, is constrained by the upper bound on the effective number of neutrino flavors $N_{\text{eff}} \leq 2.99 \pm 0.17$ [73]. This bound is then translated to a bound on η : $\eta \leq 3 \times 10^{-2}$. We will adopt three benchmarks for $\dot{\phi}_{\text{BBN}}$ corresponding to $\eta = 0$, the upper bound $\eta = 3 \times 10^{-2}$ and an illustrative intermediate value, $\eta = 10^{-4}$.

¹In relativistic units of $c = 1$, the dimension of $\kappa = 8\pi G$ is $\frac{[\text{length}]}{[\text{mass}]}$. Also, $[\alpha] = [\text{mass}][\text{length}]$, $[\gamma] = 1/[\phi] = [\sqrt{\kappa}]$. All the quantities can be written in terms of length units by appropriate factors of κ . In geometric units α is in km^2 while ϕ as well as γ are dimensionless.

²Indeed, ϕ is not a degree of freedom of the equivalent system of autonomous equations discussed in Section 4.1, and only appears when fixing the boundary conditions at BBN.

The boundary condition on $H(T_{\text{BBN}}) = H_{\text{BBN}}$ can be obtained by solving Eq. (2.4) at T_{BBN} and taking the solution closer to $H_{\text{rad}}(T_{\text{BBN}})$. At fixed η , the $\dot{\phi}_{\text{BBN}}$ linear factor that appears in the expression of ρ_{GB} can be expressed in terms of H_{BBN} through $\dot{\phi}_{\text{BBN}} = \sqrt{2\rho_\phi} = \sqrt{6\eta/\kappa}H_{\text{BBN}}$, where the sign of the square root is positive because we take $\dot{\phi}_{\text{BBN}} > 0$. Then Eq. (2.4) is equivalent to the following quadratic equation in H_{BBN}^2 :

$$8\sqrt{6\kappa\eta}f'(0)H_{\text{BBN}}^4 + (1 - \eta)H_{\text{BBN}}^2 - \frac{\kappa}{3}\rho_{\text{rad}}(T_{\text{BBN}}) = 0. \quad (3.5)$$

In Figs. 1 and 2 we show a couple of examples for the numerical solutions of the differential equations. In particular, both figures show the evolution of ρ_{rad} , ρ_ϕ , $|\rho_{\text{GB}}|$ and ρ as a function of the temperature T when $\rho_\phi(T_{\text{BBN}}) = 3 \times 10^{-2}\rho_{\text{BBN}}$ and $\tilde{\alpha} = \pm 1 \text{ km}^2$. Moreover, in Fig. 1 $\gamma = \pm 1$, while in Fig. 2 $\gamma = \pm 5$. As already pointed out, all our results are presented in terms of $\tilde{\alpha}$, i.e. we adopt the gauge $\phi(T_{\text{BBN}}) = 0$. Inspection of such figures reveals a behaviour already observed in the analysis of Ref. [1]: after a transient regime at low temperatures that can also show a high degree of nonlinearity, at large enough temperatures the energy density ρ always reaches an asymptotic regime characterized by a constant equation of state $w = p/\rho$. This is shown in more detail in Fig. 3, where in the upper panel the orange and green solid lines correspond to the evolution of w for the same parameters of Fig. 1, while the evolution of w shown in the lower panel corresponds to the parameters of Fig. 2. Moreover, in Fig. 3 the blue solid lines include also the equation of state evolution for $\rho_\phi(T_{\text{BBN}}) = 0$. In all such plots, most of the times w appears to reach either $w = -1/3$ or $w = 1$, with the exception of the cases $\tilde{\alpha} = +1 \text{ km}^2$, $\gamma = \pm 1$, for which $w \simeq 2.2$. In order to explore further this effect, a systematic evaluation of the asymptotic value of w at high temperatures is provided in Fig. 4, where the color code in each plot represents the value of w in the $\tilde{\alpha} - \gamma$ plane. In particular, the plots in the left-hand column show w at $T = 10^6 \text{ GeV}$, while those in the right-hand one show the same quantity for $T = 10^{16} \text{ GeV}$. Moreover, the plots in the first row are calculated for $\rho_\phi(T_{\text{BBN}}) = 3 \times 10^{-2}\rho_{\text{BBN}}$, those in the central row for $\rho_\phi(T_{\text{BBN}}) = 10^{-4}\rho_{\text{BBN}}$ and those in the bottom row for $\rho_\phi(T_{\text{BBN}}) = 0$.

In such plots, two effects can be clearly seen when T is large enough (and in particular in the case $T = 10^{16} \text{ GeV}$, shown in the right-hand column of Fig. 4): i) for a wide range of the $\tilde{\alpha}$ and γ parameters and for different values of $\rho_\phi(T_{\text{BBN}})$, at large temperatures the system only saturates the two values $w = 1$ and $w = -1/3$, with the exception of the small interval $-2.45 \lesssim \gamma \lesssim 2.45$ for $\tilde{\alpha} > 0$, where w varies continuously in the range $1 \lesssim w \lesssim 2.3$; ii) the boundaries of the different w domains are flat in the $\tilde{\alpha}$ parameter, i.e. the asymptotic value of w depends only on the sign of $\tilde{\alpha}$, but not on its actual value.

In the numerical analysis of Ref. [1], the asymptotic behaviours summarized above were explained in terms of Eq. (2.6) for the scalar field ϕ , and specifically by how the V'_{GB} term affects the evolution of $\dot{\phi}$ at high T . A peculiar feature of such evolution is that, with the exception of a case when it is negligibly small, ρ_{GB} turns out to be negative at high T , no matter of its sign at T_{BBN} . In particular, we note the following salient points:

- In the parameter space where $w = 1$ one observes that V'_{GB} and ρ_{GB} are exponentially suppressed and get quickly out of the game at high T , so that a standard kination

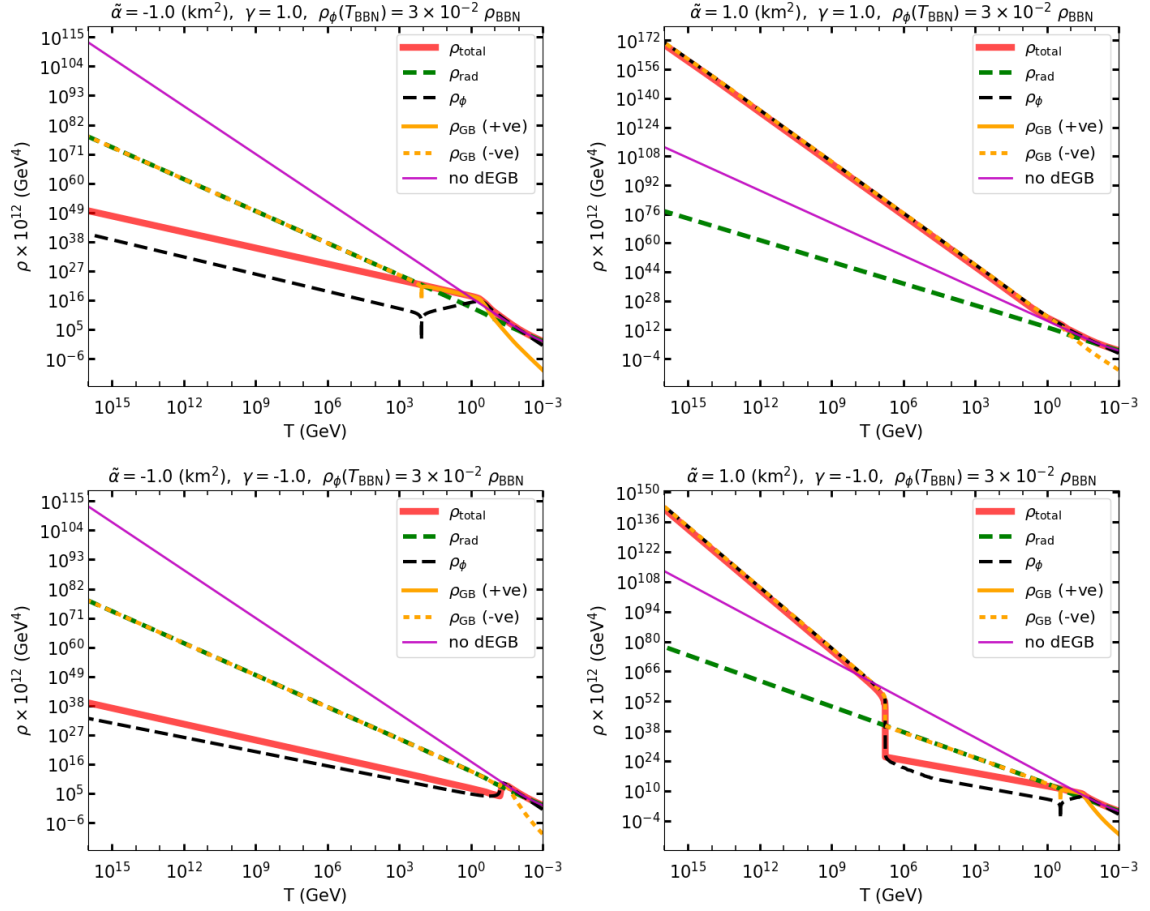


Figure 1. Evolution of ρ_{rad} , ρ_{ϕ} , ρ_{GB} and the total density ρ as a function of the temperature T , for $\tilde{\alpha} = \pm 1 \text{ km}^2$, $\gamma = \pm 1$ and $\rho_{\phi}(T_{\text{BBN}}) = 3 \times 10^{-2} \rho_{\text{BBN}}$.

scenario where ρ is driven by the kinetic energy of the scalar field is recovered (i.e. a quintessence model [12, 13, 15, 16, 74, 75] with vanishing potential $V(\phi)$).

- In the parameter space where $w = -1/3$, the V'_{GB} term mitigates and eventually stops the evolution of the scalar field at high T , so that asymptotically $\rho_{\phi}/\rho \rightarrow 0$, and $\rho \simeq \rho_{\text{rad}} + \rho_{\text{GB}}$ (we designate such regime, characterized by a subdominant $\dot{\phi}$, as “slow roll”). In such condition, $|\rho_{\text{GB}}|$ eventually tracks ρ_{rad} closely, because it grows much faster than it due to its H^3 dependence and cannot exceed it to preserve the positivity of ρ , so $|\rho_{\text{GB}}|, |\rho_{\text{GB}}| \propto T^4$. However, the sum of the two terms has a lower T dependence, $\rho \propto T^2$, due to the large cancellation between them³.
- Finally, when $1 < w \lesssim 2.3$ the V'_{GB} term accelerates the evolution of ϕ beyond standard kination at high T (we designate such regime as “fast roll”), so that $\rho \simeq$

³This peculiar cancellation will be instrumental in enhancing the GW stochastic background discussed in Section 5.

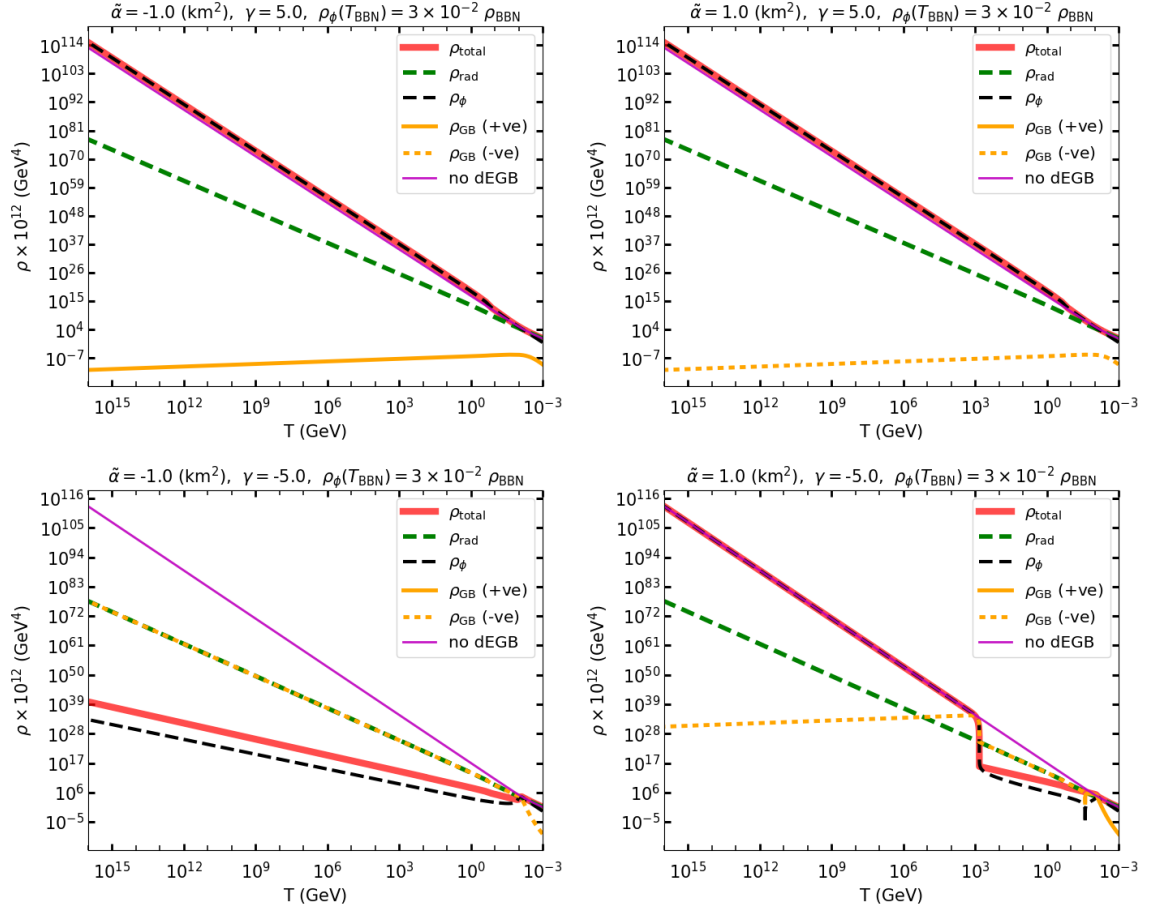


Figure 2. Same as Fig. 1, but for $\gamma = \pm 5$.

$\rho_\phi + \rho_{\text{GB}}$. Also, in this case $|\rho_{\text{GB}}|$ tracks ρ_ϕ , but the level of cancellation is not large unless $|\gamma| \rightarrow 0$.

A more detailed discussion of what summarized above can be found in Ref. [1]. In the next Section an appropriate change of variables will allow to explain all its peculiar features in a transparent way, by reformulating Eqs. (2.4, 2.5) in terms of a system of autonomous differential equations with a simple pattern of critical points and attractors.

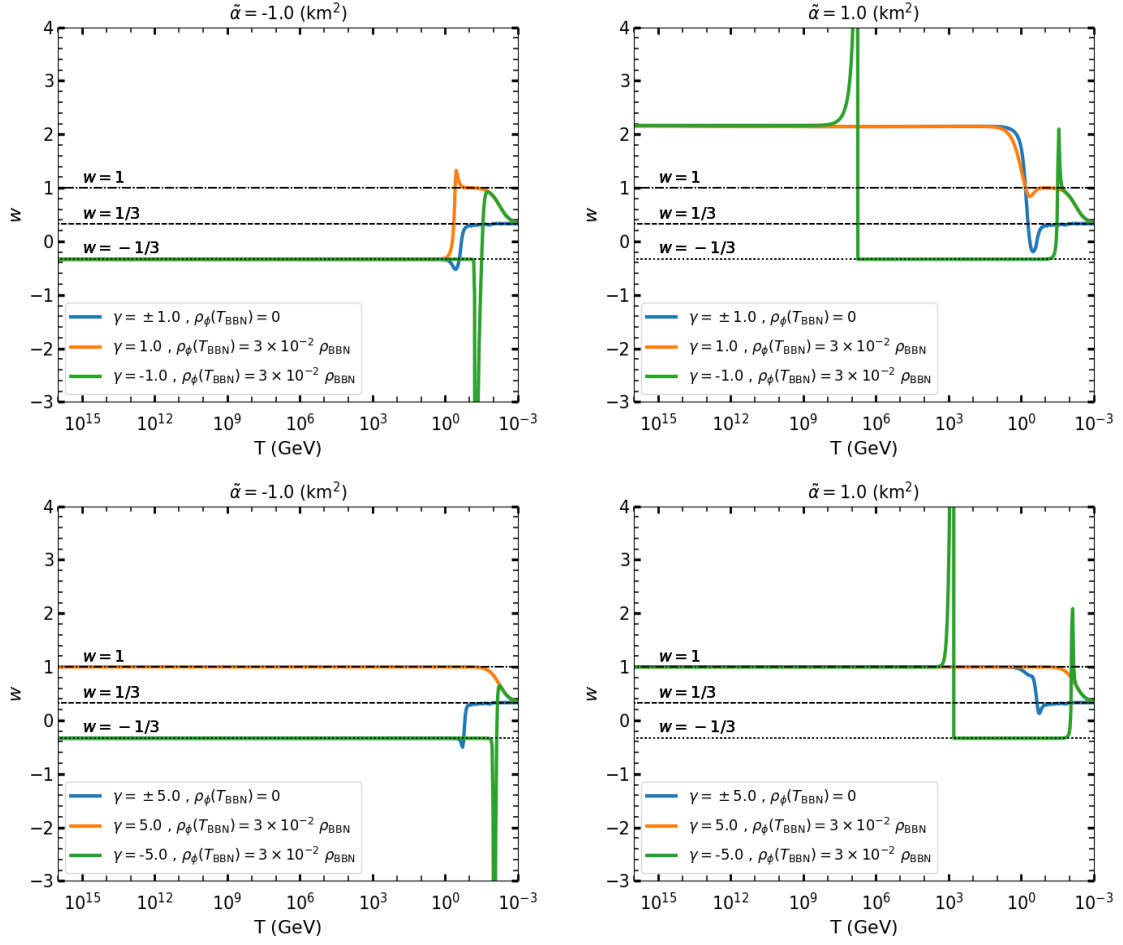


Figure 3. Evolution of the equation of state of the Universe w with T for the same parameters of Figs. 1 and 2.

4 Asymptotic behaviours

4.1 Equivalent system of autonomous equations

We start this Section by introducing the following variables [19, 76–78]:

$$\begin{aligned}
 x &\equiv \frac{\rho_\phi}{\rho} = \frac{\kappa}{6} \left(\frac{\dot{\phi}}{H} \right)^2, \\
 y &\equiv \frac{\rho_{\text{rad}}}{\rho} = \frac{\kappa g_* \pi^2}{90} \frac{T^4}{H^2}, \\
 z &\equiv \frac{\rho_{\text{GB}}}{\rho} = -8\kappa \dot{f} H = -8\kappa \frac{\partial f}{\partial \phi} \dot{\phi} H.
 \end{aligned} \tag{4.1}$$

In terms of x, y, z the system of coupled differential equations (2.5, 2.6) can then be re-expressed in the following form:

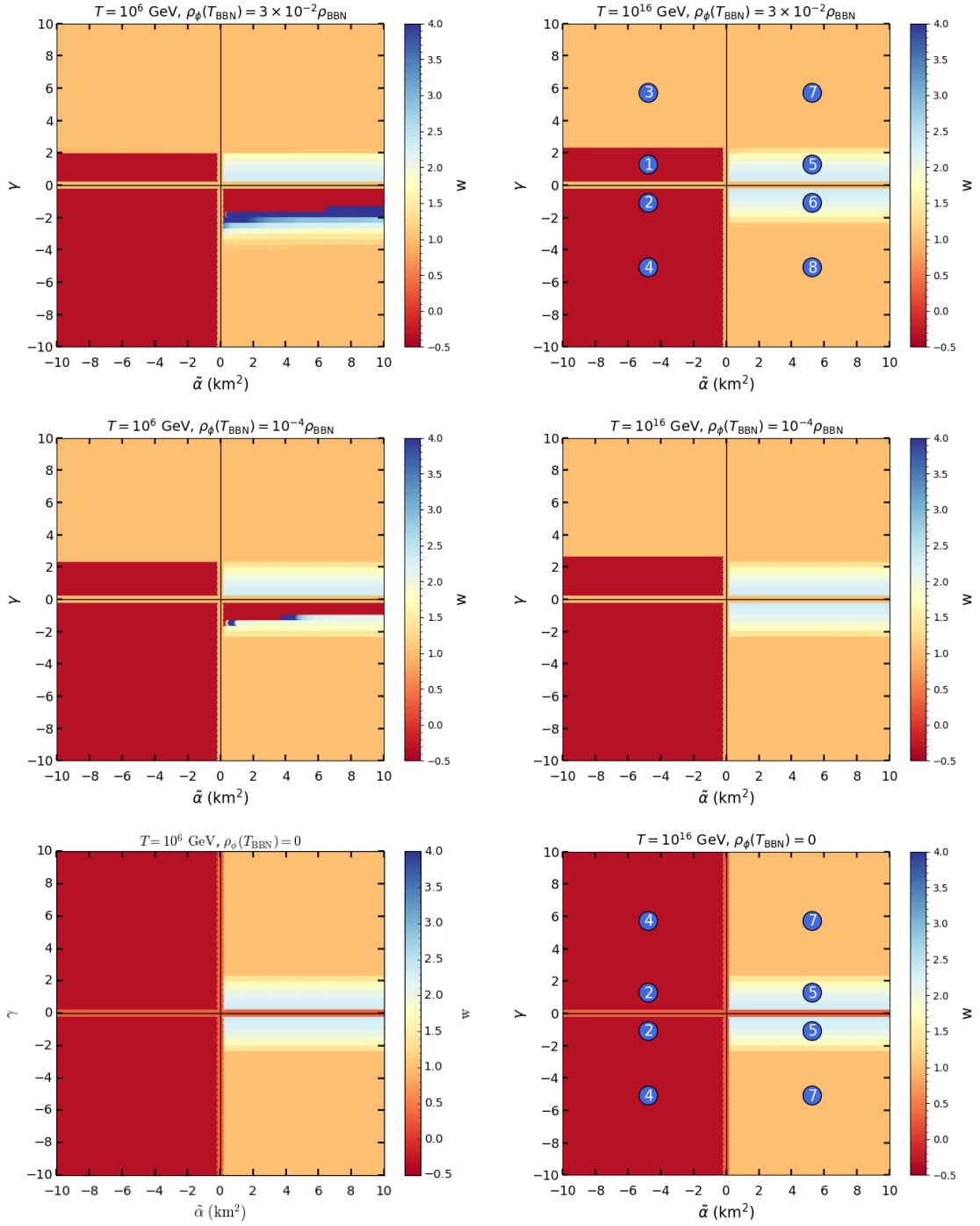


Figure 4. The color codes show the variations of the equation of state (w) of the Universe in the Gauss-Bonnet parameter space (spanned by $\tilde{\alpha}$ and γ). *Top panels:* $\rho_\phi(T_{\text{BBN}}) = 3 \times 10^{-2} \rho_{\text{BBN}}$, *middle panels:* $\rho_\phi(T_{\text{BBN}}) = 10^{-4} \rho_{\text{BBN}}$, *bottom panels:* $\rho_\phi(T_{\text{BBN}}) = 0$. *Left column:* $T = 10^6$ GeV, *right column:* $T = 10^{16}$ GeV.

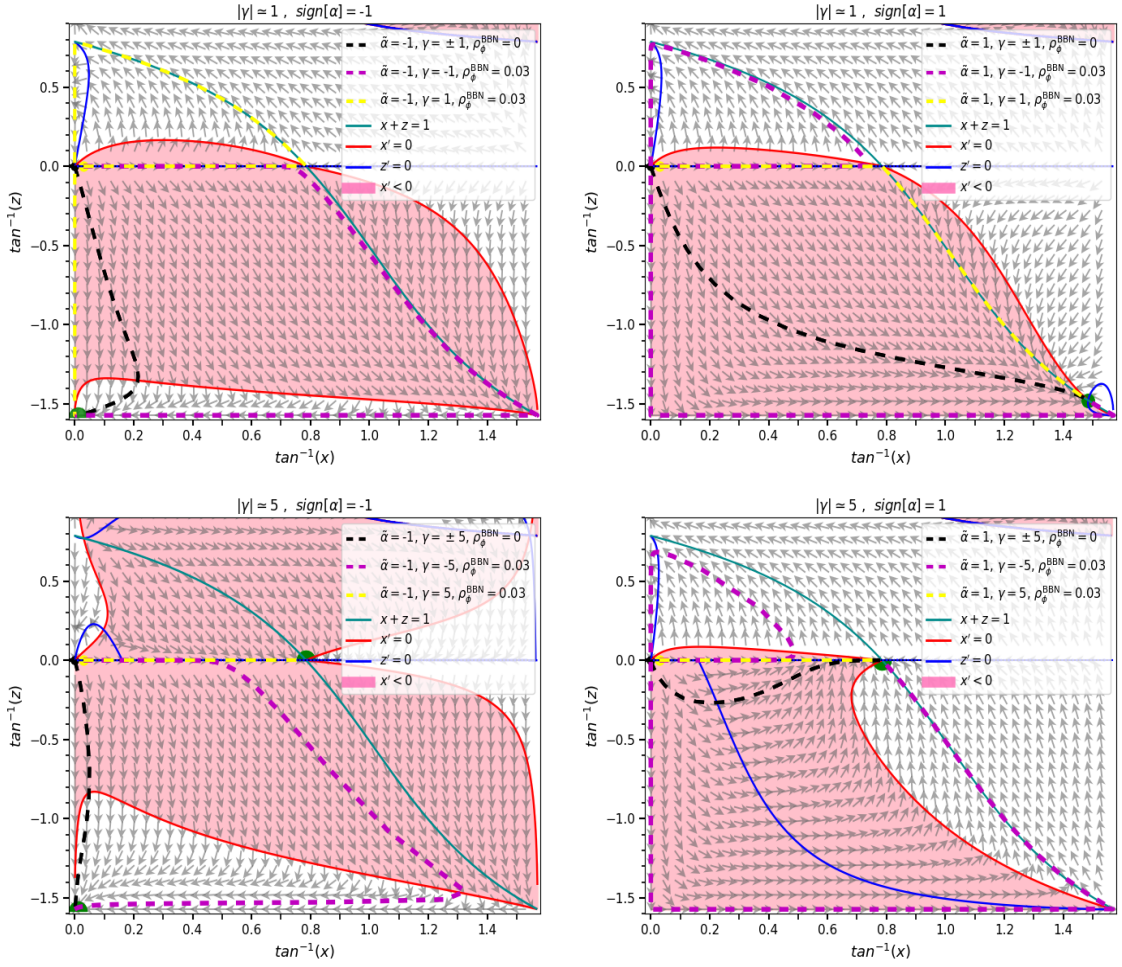


Figure 5. Examples of the evolution of Eqs (4.8, 4.9) in the (x, z) plane (in the captions $\kappa = 1$). The gray arrows in the background represent the velocity field (x', z') , while the red and the blue solid lines correspond to $x' = 0$ and $z' = 0$, respectively. The red shaded areas indicate $x' = \frac{dx}{dN} < 0$. The solid cyan line corresponds to $x + z = 1$ and the parameter space below this line is the physical one. In each case, the attractor point(s) is indicated in green.

$$\begin{aligned}
 x' &= 2x \left(\frac{\beta}{z} + \epsilon - \mu\sqrt{x} \right) = 2(\epsilon - 3)x + (\epsilon - 1)z, \\
 y' &= 2(\epsilon - 2)y, \\
 z' &= \beta - \epsilon z = 6x + 4y + (1 + \epsilon)z - 2\epsilon,
 \end{aligned} \tag{4.2}$$

where the prime indicates a derivative with respect to the e-folding parameter $N = \log(a)$ ($' = \frac{d}{dN} = \frac{d}{d \ln a} = \frac{1}{H} \frac{d}{dt}$) and

$$\beta \equiv -8\kappa\ddot{f}, \quad (4.3)$$

$$\epsilon \equiv -\frac{\dot{H}}{H^2} = 1 + q, \quad (4.4)$$

where $q = -\ddot{a}a/\dot{a}^2$ is the deceleration parameter. Moreover, we define

$$\mu \equiv \sqrt{\frac{\kappa}{6}} \frac{\partial^2 f}{\partial \phi^2} / \frac{\partial f}{\partial \phi} = \sqrt{\frac{6}{\kappa}} \gamma, \quad (4.5)$$

where in the last equality the explicit expression of f in (2.2) is used. In Eqs. (4.1) x and y are positive defined, while z can have both signs. Furthermore x , y and z verify the identities:

$$x + y + z = 1, \quad (4.6)$$

$$x' + y' + z' = 0, \quad (4.7)$$

and the system contains only two independent degrees of freedom. Choosing them to be x and z Eqs. (4.2) yield

$$x' = 2[\epsilon(x, z) - 3]x + [\epsilon(x, z) - 1]z \equiv F(x, z), \quad (4.8)$$

$$z' = 2x + [\epsilon(x, z) - 3]z + 2[2 - \epsilon(x, z)] \equiv G(x, z), \quad (4.9)$$

where $\epsilon(x, z)$ is explicitly given by

$$\epsilon(x, z) = \frac{4x^2 + 8x + z^2 + 2\sqrt{\frac{6}{\kappa}} \text{sign}(\alpha)|\gamma||z|x^{3/2}}{4x - 4xz + z^2}. \quad (4.10)$$

Note that in the equation above the appearance of the term $\text{sign}(\alpha)|\gamma||z| = \text{sign}(\alpha\gamma z)\gamma z$ is due to the fact that the change of variables $(\phi, \dot{\phi}) \rightarrow (x, z)$ requires to keep track of the sign of $\dot{\phi}$, since $z \propto \rho_{\text{GB}}$ is linear in it. Explicitly: $\dot{\phi} = \text{sign}(\dot{\phi})\sqrt{2\rho_{\phi}} = \text{sign}(\dot{\phi})H\sqrt{\frac{6}{\kappa}}x^{1/2} = -\text{sign}(\alpha\gamma z)H\sqrt{\frac{6}{\kappa}}x^{1/2}$, with $\text{sign}(\dot{\phi}) = -\text{sign}(\alpha\gamma\rho_{\text{GB}}) = -\text{sign}(\alpha\gamma z)$.

The two coupled non-linear differential equations (4.8, 4.9) are autonomous [79], i.e. they do not depend explicitly on N and describe a velocity field (x', z') in the $x - z$ plane. An explicit example of the evolution of Eqs. (4.8, 4.9) is provided in Fig. 5. In such figure, the velocity field is represented by the pattern of gray arrows in the background. The asymptotic behaviours at large T discussed in the previous Section correspond to its attractors at $N \rightarrow -\infty$, i.e. to the (x_c, z_c) configurations in the (x, z) plane for which $x' = 0, z' = 0$ (critical points) which are also stable⁴. In particular, if (x_c, z_c) is an attractor $\epsilon(x, z)$ saturates to the constant value $\epsilon(x_c, z_c)$, and this fixes the equation of state w , since the two quantities are related by

$$w = \frac{2}{3}\epsilon - 1. \quad (4.11)$$

⁴The stability of the critical points depends on the direction of the time variable in which they are solved. In our analysis we will always refer to attractors, repellers and saddle points in the case when the differential equations (4.8,4.9) are evolved from T_{BBN} to higher temperatures. This convention also fixes the direction of the velocity field shown in Fig. 5 and of the evolution patterns of Fig. 8.

So attractors explain the peculiar behaviour observed in the numerical plots of Figs. 3, where w saturates to a constant value at high T . Moreover, through $\epsilon(x, z)$ (see Eq. (4.10)) the set of autonomous differential equations (4.8, 4.9), and so its critical points, depend only on the sign of α but not on its actual value. This explains why at large-enough temperatures the equation of state domains of Fig. 4 appear as horizontal bands in the $\tilde{\alpha}$ - γ plane. In the following section we will find the critical points of Eqs. (4.8, 4.9) and discuss if/when they are stable attractors.

4.2 Finite critical points

Inverting Eqs. (4.8, 4.9) with $x' = 0, z' = 0$, we obtain the following implicit form:

$$\begin{aligned} x_c &= \frac{\epsilon - 1}{5 - \epsilon}, \\ z_c &= -2\frac{\epsilon - 3}{5 - \epsilon}, \end{aligned} \quad (4.12)$$

for the critical points. Substituting back x_c and z_c in (4.10) we obtain the following equation for ϵ :

$$(\epsilon - 1)(\epsilon - 3) \left(\sqrt{\frac{6}{\kappa}} |\gamma| \operatorname{sgn}(\alpha z_c) \sqrt{\frac{\epsilon - 1}{5 - \epsilon}} + 2\epsilon \right) = 0, \quad (4.13)$$

which has three different solutions. The first two critical points are always present and do not depend on the parameters (α, γ) . Specifically:

- $\epsilon = 3 \rightarrow (x_c, z_c) = (1, 0)$ (kination);
- $\epsilon = 1 \rightarrow (x_c, z_c) = (0, 1)$ (GB).

In the following, we will refer to them as the “kination” and the “GB” critical point (see also Table 1). On the other hand, the third critical point, that we will indicate with $(x_{\text{fp}}, z_{\text{fp}})$, is obtained by setting to zero the expression in the third parenthesis of Eq. (4.13), which vanishes only if $\operatorname{sign}(\alpha z_{\text{fp}}) < 0$. If the latter condition is verified x_{fp} and z_{fp} are given by Eq. (4.12) with ϵ being the only real solution⁵ of the cubic equation

$$2\epsilon^3 - 10\epsilon^2 + \frac{3}{\kappa}\gamma^2\epsilon - \frac{3}{\kappa}\gamma^2 = 0. \quad (4.14)$$

In both plots of Fig. 6 the orange solid line shows the equation of state $w = 2/3\epsilon - 1$ as a function of γ , with ϵ solution of Eq. (4.14). In particular Eq. (4.14) is equivalent to the condition $\sqrt{6/\kappa} |\gamma| \sqrt{x_{\text{fp}}} = 2\epsilon$, that when $w = 1$, $\epsilon = 3$ and $x_{\text{fp}} = 1$ yields $\gamma = \sqrt{6\kappa}$. Fig. 6 shows that $|\gamma| < \sqrt{6\kappa}$ when $\epsilon > 3$ and $|\gamma| > \sqrt{6\kappa}$ when $\epsilon < 3$. Then the requirement $\operatorname{sign}(\alpha z_{\text{fp}}) < 0$ implies two possibilities:

- $\alpha > 0$. In this case $z_{\text{fp}} < 0$ and $\epsilon > 3$, which requires that in Eq. (4.14) $|\gamma| < \sqrt{6\kappa}$;
- $\alpha < 0$. In this case $z_{\text{fp}} > 0$ and $\epsilon < 3$, which requires that in Eq. (4.14) $|\gamma| > \sqrt{6\kappa}$.

⁵A cubic equation $ax^3 + bx^2 + cx + d$ has one real and two complex solutions when its discriminant $\Delta = 18abcd - 4b^3d + b^2c^2 - 4ac^3 - 27a^2d^2$ is negative. The discriminant of Eq. (4.14) (with $\kappa = 1$) is $\Delta = -8\gamma^2(-27\gamma^4 + 396\gamma^2 - 1500)$ and is negative for any value of $\gamma \neq 0$.

The critical points in the x - z plane are shown in a pictorial way in Fig. 8, where the 4 possible sign combinations of α and $|\gamma| - \sqrt{6\kappa}$ are separately shown. In such figure the three critical points $(1, 0)$, $(0, 1)$ and $(x_{\text{fp}}, z_{\text{fp}})$ are represented by circles filled in green or in red color if they are stable or unstable, respectively, according to the discussion below. In particular, the $(x_{\text{fp}}, z_{\text{fp}})$ critical point lies on the $x + z = 1$ line and varies in the interval $(+\infty, -\infty) \rightarrow (1, 0)$ when $0 < |\gamma| < \sqrt{6\kappa}$ and $\alpha > 0$, while it varies in the interval $(1, 0) \rightarrow (0, 1)$ when $\sqrt{6\kappa} < |\gamma| < \infty$ and for $\alpha < 0$.

In order to determine whether a critical point $X_c = (x_c, z_c)$ is stable, one needs to expand up to linear order the velocity field $X' = (x', z')$ in its neighborhood

$$\begin{aligned} x' &= F(x, z) \simeq F(x_c, z_c) + \frac{\partial F}{\partial x}(x - x_c) + \frac{\partial F}{\partial z}(z - z_c), \\ z' &= G(x, z) \simeq G(x_c, z_c) + \frac{\partial G}{\partial x}(x - x_c) + \frac{\partial G}{\partial z}(z - z_c), \end{aligned} \quad (4.15)$$

which, using $F(x_c, z_c) = G(x_c, z_c) = 0$, is equivalent to

$$X' = J(X - X_c), \quad (4.16)$$

where

$$J = \begin{pmatrix} \frac{\partial F}{\partial x} & \frac{\partial F}{\partial z} \\ \frac{\partial G}{\partial x} & \frac{\partial G}{\partial z} \end{pmatrix}_{(x,z)=(x_c,z_c)}. \quad (4.17)$$

X_c is a stable attractor for $N \rightarrow -\infty$ if the eigenvalues of the Jacobian J are both positive. It is explicitly given by

$$J = \begin{pmatrix} 2[\epsilon(x_c, z_c) - 3] & \epsilon(x_c, z_c) - 1 \\ 2 & \epsilon(x_c, z_c) - 3 \end{pmatrix} + (x_c + 1) \begin{pmatrix} \frac{\partial \epsilon}{\partial x} & \frac{\partial \epsilon}{\partial z} \\ -\frac{\partial \epsilon}{\partial x} & -\frac{\partial \epsilon}{\partial z} \end{pmatrix}_{(x,z)=(x_c,z_c)}, \quad (4.18)$$

where

$$\frac{\partial \epsilon}{\partial x} = \frac{3\sqrt{\frac{6}{\kappa}} \text{sgn}(\alpha z) |\gamma| x^{1/2} z + 8x + 8 + 4(z-1)\epsilon}{4x - 4xz + z^2}, \quad (4.19)$$

$$\frac{\partial \epsilon}{\partial z} = \frac{2\sqrt{\frac{6}{\kappa}} \text{sgn}(\alpha z) |\gamma| x^{3/2} + 2z + (4x - 2z)\epsilon}{4x - 4xz + z^2}. \quad (4.20)$$

In particular, substituting $(x_c, z_c) = (0, 1)$ in Eq. (4.18) J yields

$$J = \begin{pmatrix} 4 & 0 \\ -6 & -2 \end{pmatrix}.$$

Eigenvalues : $\lambda_1 = 4, \quad \lambda_2 = -2,$

Eigenstates : $v_1 = [1/\sqrt{2}, -1/\sqrt{2}], \quad v_2 = [0, 1],$ (4.21)

so that the critical point $(0, 1)$ is a saddle point and is not stable. For this reason, in Fig. 8 the corresponding circle is always filled in red color⁶. On the other hand, substituting $(x_c, z_c) = (1, 0)$ one gets

$$J = \begin{pmatrix} 2 & \text{sign}(\alpha z) \sqrt{\frac{6}{\kappa}} |\gamma| + 8 \\ 0 & -\text{sign}(\alpha z) \sqrt{\frac{6}{\kappa}} |\gamma| - 6 \end{pmatrix},$$

$$\text{Eigenvalues : } \lambda_1 = 2, \quad \lambda_2 = -6 - \text{sign}(\alpha z) \sqrt{\frac{6}{\kappa}} |\gamma|,$$

$$\text{Eigenstates : } v_1 = [1, 0] \quad v_2 = [0, 1]. \quad (4.22)$$

In this case $(1, 0)$ is an attractor (i.e. both eigenvalues are positive) if $\text{sign}(\alpha z) |\gamma| < -\sqrt{6\kappa}$, i.e. if $\text{sign}(\alpha z) < 0$ and $|\gamma| > \sqrt{6\kappa}$. In other words:

$$|\gamma| < \sqrt{6\kappa} \rightarrow \text{saddle point},$$

$$|\gamma| > \sqrt{6\kappa} \rightarrow \begin{cases} \alpha > 0 & \begin{cases} z \rightarrow 0^+ & \text{saddle point} \\ z \rightarrow 0^- & \text{attractor} \end{cases} \\ \alpha < 0 & \begin{cases} z \rightarrow 0^+ & \text{attractor} \\ z \rightarrow 0^- & \text{saddle point.} \end{cases} \end{cases} \quad (4.23)$$

As a consequence, in Fig. 8 the circle corresponding to the critical point $(1, 0)$ is filled in red (saddle point) when $|\gamma| < \sqrt{6\kappa}$ while it is filled in red/green in its positive/negative half depending on the sign of α .

As far as the critical point (x_{fp}, z_{fp}) is concerned, the analytic expressions of the Jacobian J eigenvalues are cumbersome, so we provide a plot of their numerical values in Fig. 7. From this figure one can see that the two eigenvalues of the Jacobian are both positive (and, as a consequence, the critical point (x_{fp}, z_{fp}) is a stable attractor) only when $\alpha > 0$ and $|\gamma| < \sqrt{6\kappa}$. Specifically, in the interval $0 \leq |\gamma| \leq \sqrt{6\kappa}$ Eq. (4.14) yields $3 \leq \epsilon \leq 5$, which using Eq. (4.11) corresponds to the interval $1 \leq w \leq 7/3$ for the equation of state. This explains the upper bound $w \lesssim 2.3$ observed in the numerical analysis of Ref. [1] and in Section 3 for $\alpha > 0$ and $|\gamma| \rightarrow 0$. In Table 1 we refer to this attractor as “fast-roll”. On the other hand, when $|\gamma| > \sqrt{6\kappa}$ and $\alpha < 0$ such critical point is not stable, because either one or both the eigenvalues of the Jacobian are negative. The situation is again summarized schematically in Fig. 8, where (x_{fp}, z_{fp}) is represented with a green dot (attractor) for $\alpha > 0$ and $|\gamma| < \sqrt{6\kappa}$, with a red dot for $\alpha < 0$ and $|\gamma| > \sqrt{6\kappa}$, while it is missing in the remaining cases when (x_{fp}, z_{fp}) is not a critical point in the first place (i.e. for $\alpha > 0$ and $|\gamma| > \sqrt{6\kappa}$ or $\alpha < 0$ and $|\gamma| < \sqrt{6\kappa}$).

Combining the discussion of the critical points $(1, 0)$ and (x_{fp}, z_{fp}) it is now possible to understand why in Fig. 6 for $\alpha > 0$ the equation of state of the numerical solutions of the full system of differential equations (2.4, 2.5, 2.6) tracks the analytical solution of the

⁶One should notice that the critical point $(0, 1)$ is not physical, because $x = 0$ implies $\dot{\phi} = 0$ and so also $z = \rho_{GB} = 0$.

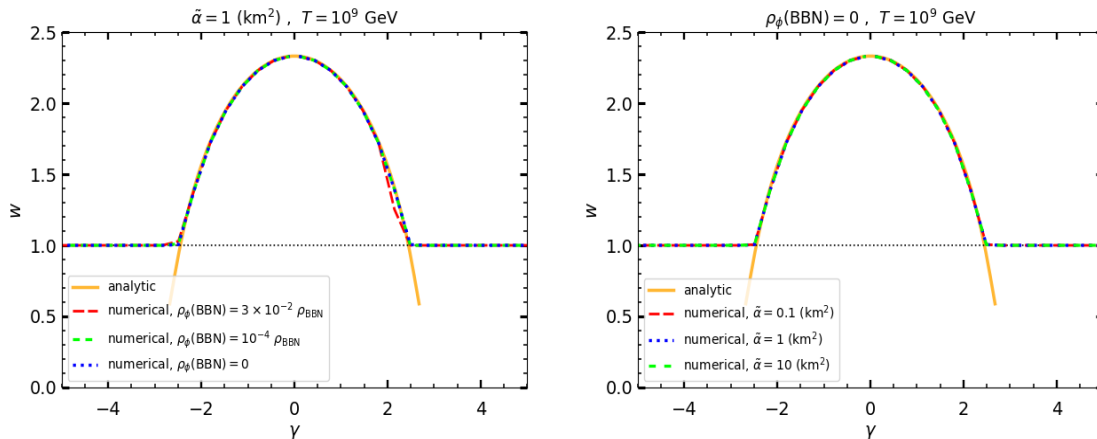


Figure 6. Equation of state w for the critical point $(x_{\text{fp}}, z_{\text{fp}})$ as a function of γ and for $\alpha > 0$. In the caption $\kappa = 1$. The yellow solid line represents the equation of state w calculated using the solution of the cubic equation (4.14). The other curves correspond to the numerical solution of the full set of Eqs. (2.4, 2.5, 2.6). *Left:* for different values of $\rho_\phi(T_{\text{BBN}})$; *Right:* for different values of $\tilde{\alpha}$.

cubic equation (4.14) for $|\gamma| < \sqrt{6\kappa}$, so that in such case $1 < w < 7/3$, while for $|\gamma| > \sqrt{6\kappa}$ it saturates to $w = 1$. In fact, in the schematic summary of Fig. 8 one can see that when $\alpha > 0$ and $|\gamma| < \sqrt{6\kappa}$ (tracks ⑤ and ⑥ in Figs. 4 and 8) the only stable critical point of the system is $(x_{\text{fp}}, z_{\text{fp}})$, while for $|\gamma| > \sqrt{6\kappa}$ it is $(1, 0)$ (for $z \rightarrow 0^-$, see tracks ⑦ and ⑧ in the same figures).

As a comment one can also point out that from Fig. 7 one can see that $(x_{\text{fp}}, z_{\text{fp}})$ is a saddle point (with $\lambda_{\text{max}} > 0$ and $\lambda_{\text{min}} < 0$) for $\sqrt{6\kappa} < |\gamma| < \sqrt{8\kappa}$, corresponding to $1/3 < w < 1$, while it is a repelling node (with both negative eigenvalues, $\lambda_{\text{max}}, \lambda_{\text{min}} < 0$) for $|\gamma| > \sqrt{8\kappa}$, corresponding to $-1/3 < w < 1/3$. In particular, when $(x_{\text{fp}}, z_{\text{fp}})$ is a saddle point one of the two normal modes corresponds to an unstable attractor, that can be achieved by a tuning of the boundary conditions. However, such attractor is only possible when $w > 1/3$, while for $w < 1/3$ such unstable solution disappears. Why this transition happens for $w = 1/3$, corresponding to the equation of state of radiation, can be understood in the following way. The right-hand plot of Fig. 7 shows the angle between the approaching path to $(x_{\text{fp}}, z_{\text{fp}})$ of each normal mode of the linearized differential equation (4.16) and the x axis. Such angle is never $-\pi/4$, i.e. the normal modes are always outside the path along the $x + z = 1$ line. Formally, this means that the boundary condition to obtain both normal modes always requires $x + y < 1$ and $y > 0$. Physically, this means that such asymptotic cosmological solution requires a non-vanishing radiation density at lower temperatures. This includes the case of the unstable attractor corresponding to $\lambda_{\text{max}} > 0$. Such a solution is only possible if the expansion rate of the Universe is faster than that of radiation, i.e. for $w > 1/3$. On the other hand, when $w < 1/3$ radiation is bound to eventually dominate at high temperature, and, even at the cost of tuning, such $(x_{\text{fp}}, z_{\text{fp}})$ solution is not achievable anymore. As a consequence, also the second eigenvalue in the

left-hand plot of Fig. 7 turns negative. This is at variance with what happens to the case of the $(0, 1)$ saddle point discussed before, which has an asymptotic equation of state as low as $w = -1/3$, corresponding to an expansion rate slower than radiation. In this case, the direction of the unstable attractor that corresponds to the positive eigenvalue $\lambda = 4$ is along the line $x + z = 1$ (see Eq.(4.21)) requiring, identically $y = \rho_{\text{rad}} = 0$. Physically, such cosmological solution at $T \rightarrow \infty$ requires that the radiation density exactly vanishes at some lower temperature so that the corresponding expansion rate $\rho \propto T^2$ is not overtaken at high temperature by that of radiation, $\rho_{\text{rad}} \propto T^4$.

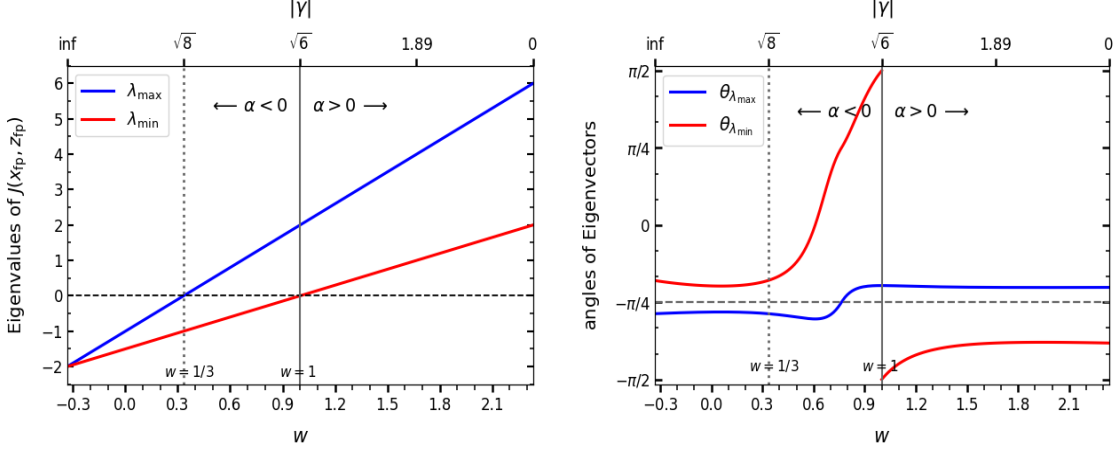


Figure 7. Eigenvalues of the Jacobian $J(x_{\text{fp}}, z_{\text{fp}})$ for the critical point $(x_{\text{fp}}, z_{\text{fp}})$, defined by Eq. (4.12) with ϵ solution of the cubic equation (4.14) (in the plot $\kappa = 1$). The vertical dotted line corresponds to $|\gamma| = \sqrt{8\kappa} \simeq 2.83$, $\epsilon = 2$ and $w = 1/3$, while the vertical solid line corresponds to $|\gamma| = \sqrt{6\kappa} \simeq 2.45$, $\epsilon = 3$ and $w = 1$. Notice that $(x_{\text{fp}}, z_{\text{fp}})$ is a critical point only for $\gamma < \sqrt{6\kappa}$ when $\alpha > 0$, and for $\gamma > \sqrt{6\kappa}$ when $\alpha < 0$ (see schematic view of Fig. 8).

4.3 Critical points at infinity

In the previous Section when $|\gamma| \rightarrow 0$ Eq. (4.14) yields $\epsilon \rightarrow 5$ and in Eq. (4.12) the critical point $(x_{\text{fp}}, z_{\text{fp}})$ is driven to $(+\infty, -\infty)$ along the line $x + z = 1$, with $w \rightarrow 7/3$. In this case $\rho_\phi \rightarrow \infty$ and $\rho_{\text{GB}} \rightarrow -\infty$, with a large cancellation between the two, so that the total density remains finite, while at the same time $\rho_{\text{rad}}/\rho \rightarrow 0$. This effect is possible because ρ_{GB} can grow negative at high temperature.

Something analogous happens when at high temperature a large cancellation occurs between $\rho_{\text{rad}} \rightarrow \infty$ and $\rho_{\text{GB}} \rightarrow -\infty$ while, at the same time, $\rho_\phi/\rho \rightarrow 0$. In order to see that this can be a stable regime at high temperature one can expand Eq. (4.10) in the leading term $\mathcal{O}(x/z) \rightarrow 0$, obtaining

$$\begin{aligned} \epsilon &= \frac{1 + \mathcal{O}(x^{3/2}/z)}{1 - 4x/z + \mathcal{O}(x/z^2)} \simeq 1 + 4\frac{x}{z} \\ \Rightarrow (\epsilon - 1)z &\rightarrow 4x, \end{aligned} \tag{4.24}$$

	(x, z)	$0 < \gamma < \sqrt{6\kappa}$	$\sqrt{6\kappa} < \gamma < \infty$
Kination	$(1, 0)$	Saddle point	Attractor ($\alpha z < 0$) ③, ⑦, ⑧ Saddle point ($\alpha z > 0$)
GB	$(0, 1)$	Saddle point	
Fast roll	$(x_{\text{fp}}, z_{\text{fp}})$	Attractor ($\alpha > 0$) ⑤, ⑥	Saddle point ($\alpha < 0, \gamma < \sqrt{8\kappa}$) Repulsive node ($\alpha < 0, \gamma > \sqrt{8\kappa}$)
Slow roll	$(0, -\infty)$	Attractor ($\alpha < 0$) ①, ②, ④ Saddle point ($\alpha > 0$)	

Table 1. Summary of the critical points discussed in Sections 4.2 and 4.3. Next to each attractor the circled number indicates the flows shown schematically in Fig. 8. The same numbers are also shown in the different domains of Fig. 4 for the equation of state.

which implies $\epsilon \rightarrow 1$ and $w \rightarrow -1/3$, while, at the same time, $x' = 0$ (when the equation above is used in (4.8)). This slow-roll regime for the scalar field was already discussed in [1], and has the peculiarity that $\rho_{\text{rad}}, |\rho_{\text{GB}}| \propto T^4$ but $\rho_{\text{rad}} + \rho_{\text{GB}} \propto T^{3(1+w)} \propto T^2$, with a large cancellation between ρ_{rad} and ρ_{GB} . Indeed, combining $x' = 0$ with Eq. (4.7) implies $(y + z)' = 0$, while at the same time for $\epsilon \rightarrow 1$ one has $y' = -2y \neq 0$ from Eq. (4.2). As a consequence both $y' \simeq -z' \neq 0$ but $y' + z' = 0$. In order to understand if such critical point at infinity is stable one needs to extend the expansion (4.24) to the next-to-leading term $\mathcal{O}(x^{3/2}/z)$:

$$\begin{aligned} \epsilon &= 1 + 4\frac{x}{z} + 2\text{sign}(\alpha z) \sqrt{\frac{6}{\kappa}} |\gamma| \frac{x^{3/2}}{z} + \mathcal{O}\left(\frac{x}{z^2}\right) \\ \Rightarrow (\epsilon - 1)z &\rightarrow 4x + 2\text{sign}(\alpha z) \sqrt{\frac{6}{\kappa}} |\gamma| x^{3/2}, \end{aligned} \quad (4.25)$$

in order to get x' from (4.8). Moreover, setting $t = 1/z$ in Eqs. (4.8, 4.9) the two variables (x, t) decouple close to the critical point $(x, t) = (0, 0)$

$$x' = 2\text{sign}(\alpha t) \sqrt{\frac{6}{\kappa}} |\gamma| x^{3/2}, \quad (4.26)$$

$$t' = 2t. \quad (4.27)$$

The equation above shows that $(x, t) = (0, 0^-)$ ($(x, z) = (0, -\infty)$) is an attractor when $\text{sign}(\alpha) < 0$ and a saddle point when $\text{sign}(\alpha) > 0$. In Fig. 8 this is schematically represented by the arrows pointing either toward the negative z axis or away from it. A summary of the critical points discussed in the last two Sections is provided in Table 1.

4.4 Flows of the autonomous equation

The asymptotic behaviour of the equation of state shown in Fig. 4 has a clear interpretation in the discussion of Sections 4.2 and 4.3 about the attractors of the autonomous

system of differential equations (4.8, 4.9). In particular, the plots of Fig. 8 provide a qualitative explanation of how the different attractors are approached depending on the boundary conditions.

We start our discussion by analysing the behaviour of the differential equations in the origin. In particular, one can notice that the mapping between the differential equations of Eqs. (2.4, 2.5, 2.6) and those of Eqs. (4.8, 4.9) presents there a degeneracy, since the ϵ function defined in Eq. (4.10) is undetermined for $(x, z) = (0, 0)$. In particular, from the point of view of Eqs. (4.8, 4.9) the two variables x and z are independent, and the value of ϵ in the origin depends on the specific flow line followed by the system to approach it⁷. However, from their definition (4.1) it is clear that x and z are correlated in the origin, since they can only vanish together when $\dot{\phi} \rightarrow 0$. In particular, to calculate ϵ in the origin one can use the explicit expressions of x and z in terms of ρ_ϕ and ρ_{GB} :

$$\lim_{x, z \rightarrow 0} \epsilon(x, z) = \frac{8 + \frac{z^2}{x}}{4 + \frac{z^2}{x}}, \quad (4.28)$$

$$\frac{z^2}{x} = \frac{\rho_{\text{GB}}^2}{\rho_\phi} = 384\kappa (f')^2 H^4 \simeq (8\pi)^2 0.14g_*^2 \left(\frac{\alpha}{\text{km}^2}\right)^2 \gamma^2 e^{2\gamma\phi} \left(\frac{T}{\text{GeV}}\right)^8, \quad (4.29)$$

which shows that (i) in the origin ϵ is well defined, since in the z^2/x combination $\dot{\phi} \rightarrow 0$ cancels out (this needs to be the case since nothing special happens for $\dot{\phi} = 0$ in the original Friedmann equations (2.4, 2.5, 2.6)); (ii) the actual value of $\epsilon(0, 0)$ depends on the previous evolution history of the system; (iii) the quantity z^2/x is extremely sensitive to the temperature. At this stage it is convenient to divide the discussion in two cases, depending on the value of $\rho_\phi(T_{\text{BBN}})$.

- $\rho_\phi(T_{\text{BBN}}) = 0$.

When $\dot{\phi}$ is set to zero at BBN ($T = 1$ MeV) the flow originates from the $(0, 0)$ point and in Eq. (4.29) $z^2/x \ll 1$ so that $\epsilon \rightarrow 2$ and $w = 1/3$, i.e. standard Cosmology is recovered. Moreover, Eq. (4.9) yields $(z')_{\text{BBN}} \simeq z^2/(2x) > 0$, and since we evolve the differential equations in the negative e-folding direction this implies that z grows negative. In other words, if the system starts from the origin it can only evolve to the negative z plane, following one of the paths that in Fig. 8 are indicated with the numbers ②, ⑤, ④ and ⑦ (this explains why in the last row of Fig. 4, corresponding to $\rho_\phi(T_{\text{BBN}}) = 0$, only such numbers appear). For all combinations of $\tilde{\alpha}$ and γ , there is always an attractor in the $z < 0$ plane, so the system quickly converges to it. In particular, for $\tilde{\alpha} < 0$ the attractor is the slow-roll solution $(0, -\infty)$ with $w = -1/3$, while for $\tilde{\alpha} > 0$ the attractor is either $(x_{\text{fp}}, z_{\text{fp}})$ with $1 < w < 7/3$ when $|\gamma| < \sqrt{6\kappa}$ (fast roll) or $(1, 0)$ with $w = 1$ when $|\gamma| > \sqrt{6\kappa}$ (kination). As already pointed out, such results are symmetric with respect to the sign of the parameter γ , as it is observed, for instance, in the plots of the last row of Fig. 4.

⁷In the origin an infinite set of different flows of the autonomous equations (4.8, 4.9) converge. However each solution through the origin is unique for a given set of boundary conditions (i.e. Eqs. (4.8, 4.9) satisfy the Cauchy–Lipschitz theorem [79]).

- $\rho_\phi(T_{\text{BBN}}) > 0$.

In this case, the flow originates from $(x_{\text{BBN}}, z_{\text{BBN}})$, with the initial sign of z_{BBN} depending on the boundary conditions. In particular for our choice $\dot{\phi}(T_{\text{BBN}}) > 0$ for $\tilde{\alpha}\gamma > 0$ one has $z_{\text{BBN}} < 0$ and qualitatively the evolution of the system is very similar to the case for $\rho_\phi(T_{\text{BBN}}) = 0$ already discussed (the boundary conditions at BBN “go with the flow”, see trajectories ②, ⑤, ④ and ⑦ in Fig. 8). This is confirmed by the plots of Fig. 4, that indeed when $\dot{\phi}(T_{\text{BBN}}) > 0$ for $\tilde{\alpha}\gamma > 0$ look similar to those for which $\dot{\phi}(T_{\text{BBN}}) = 0$. On the other hand, a different situation emerges when $\tilde{\alpha}\gamma < 0$ and $z_{\text{BBN}} > 0$. From Table 1 and Fig. 8 one can see that in most cases the only attractor of the system is in the negative z plane. In such cases the boundary conditions at BBN “kick the flow in the wrong direction” so that after a transient path in the $z > 0$ plane (see paths ①, ⑥ and ⑧ in Fig. 8) the system needs to evolve from the positive z plane to the negative z plane. This can only happen by crossing the origin and explains the cases where $\dot{\phi}$ is observed to change sign at high temperature (in Figs. 1 and 2 this happens when both ρ_ϕ and ρ_{GB} vanish). In such situations the system is required to take a large “detour” in the positive plane before reaching a trajectory tangent to the z axis that allows it to cross the origin. According to Eq. (4.29) now when $\dot{\phi} \rightarrow 0$ one has $z^2/x \gg 1$ and $\epsilon \rightarrow 1$, i.e. the equation of state corresponds to slow-roll, $w = -1/3$. For $\tilde{\alpha} < 0$ and $\gamma < \sqrt{6\kappa}$ this is also the only available attractor, so w does not change anymore. On the other hand, for $\tilde{\alpha} > 0$ slow-roll is a saddle point, so that $w = -1/3$ is only a metastable solution: the system follows $w = -1/3$ for a while and then eventually jumps to the real attractor at higher temperatures, which is $(x_{\text{fp}}, z_{\text{fp}})$ for $|\gamma| < \sqrt{6\kappa}$ and $(1, 0)$ for $|\gamma| > \sqrt{6\kappa}$ ⁸. As far as the asymptotic equation of state is concerned, this implies that for $\tilde{\alpha} > 0$ the plots of Fig. 4 are very similar to the $\dot{\phi}(T_{\text{BBN}}) = 0$ case. The only exception to this behaviour corresponds to $\tilde{\alpha} < 0$ and $\gamma > \sqrt{6\kappa}$. In this case, a new attractor appears at $(1, z \rightarrow 0^+)$, i.e. in the *positive* plane, so that, instead of crossing the origin and reaching slow-roll, the system quickly asymptotizes to kination (see track ③ in Fig. 8). This explains why in Fig. 4 for $\tilde{\alpha} < 0$ the equation of state turns from slow-roll ($w = -1/3$) to kination ($w = 1$) for $\gamma > \sqrt{6\kappa}$ when $\dot{\phi}(T_{\text{BBN}}) > 0$, while it is always slow-roll when $\dot{\phi}(T_{\text{BBN}}) = 0$. We conclude by pointing out that also kination can be a metastable regime, for those trajectories that approach the $(1, 0)$ saddle point before eventually moving to another attractor (see tracks ①, ②, ⑤, ⑥ and ⑧ in Fig. 8). In such case the system follows $w = 1$ for a while and then eventually jumps to the real attractor at higher temperatures. The appearance of such metastable solutions for the equation of state, which are clearly visible in Fig. 3 and also in Fig. 13, can have important consequences for the GW stochastic background discussed in Section 5, which depends not only on the asymptotic behaviour at high temperature but on the whole expansion history of the Universe.

⁸Indeed, in the analysis Ref. [1] the evolution of the dEGB Friedmann equations was limited to the temperatures relevant for WIMP thermal decoupling, and the case $\tilde{\alpha} > 0$, $\gamma < 0$ was mistakenly assumed to have the slow-roll asymptotic behaviour, missing the transition to a different w at higher temperatures.

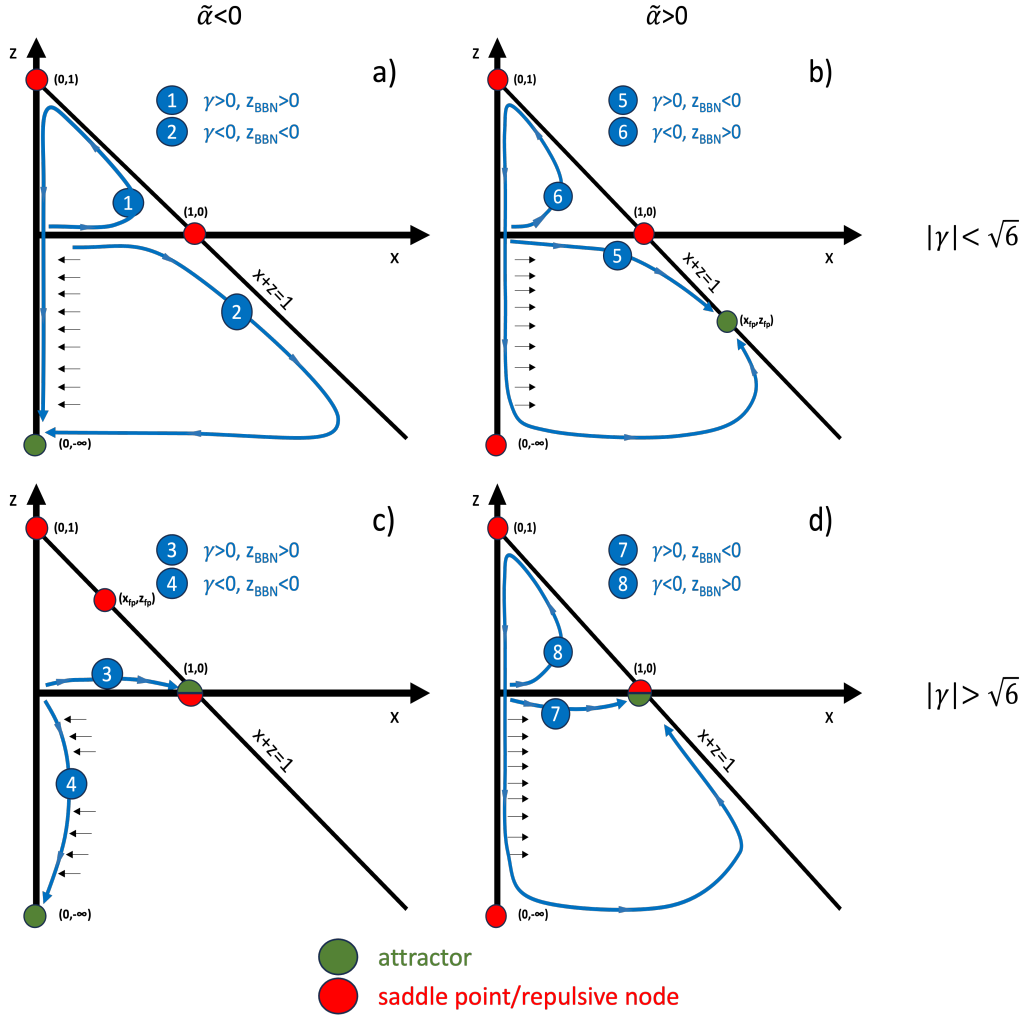


Figure 8. Schematic description of the critical points and of the qualitative evolution of the autonomous differential equations (4.8, 4.9) (in the caption $\kappa = 1$). Circles filled in green or red represent stable and unstable critical points, respectively. In the case of $(x_c, z_c) = (1, 0)$ only half of the circle is filled in green, depending on whether the point is an attractor for $z \rightarrow 0^+$ or $z \rightarrow 0^-$ (see text). The flows numbered from ① to ⑧ correspond to the eight paths that exhaust the possible high-temperature evolution of dEGB Cosmology. The same numbers are shown in Fig. 4.

5 Constraints from Gravitational Waves

5.1 GW stochastic background

5.1.1 Theoretical framework

Any plasma of relativistic particles in thermal equilibrium emits a stochastic background of gravitational waves, which in the case of the Standard Model is expected to peak at a frequency of around 80 GHz [67, 68]. At variance with other hypothetical GW sources such as scenarios of inflation, reheating models and phase transitions in GUT theories, such process is an irreducible source of GWs that only involves standard physics, and po-

tentially represents an unambiguous way to directly probe Cosmological models before Big Bang Nucleosynthesis. So, although present detectors are only sensitive to frequencies of the order of few Hertz, some proposals exist to extend the experimental reach to the GHz range [69, 70].

The magnitude and spectral shape of the corresponding stochastic GW background that is produced during the history of the Universe from the beginning of the thermal-radiation dominated epoch after the big bang until the electroweak crossover, at a temperature $T_{\text{EWCO}} = 160$ GeV, has been calculated in [67, 68]. At a given time it can be expressed as

$$\frac{1}{a^4} \frac{d}{dt} (a^4 \rho_{\text{GW}}(t)) = \left(\frac{\partial}{\partial t} + 4H \right) \rho_{\text{GW}}(t) = 4 \frac{T^4}{M_{\text{PL}}^2} \int \frac{d^3 k}{(2\pi)^3} \eta(T, k), \quad (5.1)$$

where $\eta(k, T)$ is the shear viscosity of the SM plasma. The equation above neglects the back reaction contribution from gravitational excitations annihilating or decaying back into the plasma, which is a good approximation for temperatures below the Planck scale. In Eq. (5.1) the right-hand side encodes the information related to the GW production, which is modeled by the function $\eta(k, T)$, while the left-hand side describes the evolution of $\rho(t)_{\text{GW}}$ according to the Cosmological model and, in particular, to the temperature dependence of the Hubble parameter.

For a plasma kept in thermal equilibrium by SM interactions, $\eta(k, T)$ is a function of $\hat{k} = k/T$ and T given by

$$\eta(\hat{k}, T) = \begin{cases} \frac{1}{8\pi} \frac{16}{g_1^4 \ln(5T/m_{D_1})}, & k \lesssim \alpha_1^2 T, \\ \eta_{\text{HTL}}(\hat{k}, T) + \eta^T(\hat{k}, T), & k \gtrsim 3T, \end{cases}, \quad (5.2)$$

where $\alpha_1 = g_1^2/4\pi$ with g_1 the weak-hypercharge coupling and $\eta_{\text{HTL}}(\hat{k}, T)$ is the so called Hard Thermal Logarithmic (HTL) expression [68, 80]:

$$\eta_{\text{HTL}}(\hat{k}, T) = \frac{1}{16\pi} \hat{k} n_B(\hat{k}) \sum_{i=1}^3 \hat{m}_{D_i}^2 \ln \left(4 \frac{1}{\hat{m}_{D_i}^2} \hat{k}^2 + 1 \right), \quad (5.3)$$

where $n_B(\hat{k}) = \frac{1}{e^{\hat{k}} - 1}$, and the Debye masses are given by

$$\hat{m}_{D_i} = \frac{m_{D_i}}{T}, \quad m_{D_i}^2 = \begin{cases} d_1 \frac{11}{6} g_1^2 T^2, & d_1 = 1, \\ d_2 \frac{11}{6} g_2^2 T^2, & d_2 = 3, \\ d_3 2g_3^2 T^2, & d_3 = 8. \end{cases}, \quad (5.4)$$

In Eq. (5.2) $\eta^T(\hat{k}, T)$ represents the contribution from the thermal corrections computed in [68] and is given by

$$\begin{aligned} \eta^T(\hat{k}, T) = & [3g_2^2(T) + 12g_3^2(T)] \eta_{gg}(\hat{k}) + [g_1^2(T) + 3g_2^2(T)] \eta_{sg}(\hat{k}) \\ & + [5g_1^2(T) + 9g_2^2(T) + 24g_3^2(T)] \eta_{fg}(\hat{k}) \\ & + [3|y_t(T)|^2 + 3|y_b(T)|^2 + |y_\tau(T)|^2] \eta_{sf}(\hat{k}). \end{aligned} \quad (5.5)$$

In the expression above, the couplings g_i of the SM gauge group $SU(3)_c \times SU(2)_L \times U(1)_Y$ and the Yukawa couplings y_t , y_b and y_τ depend on the temperature, with y_b and y_τ giving a negligible contribution. In Appendix A, we provide the functions $\eta_{gg}(\hat{k})$, $\eta_{sg}(\hat{k})$, $\eta_{fg}(\hat{k})$ and $\eta_{sf}(\hat{k})$ in the notation of [81], and correct a typo in one of them.

In the next Section, we will use the numerical solutions discussed in Section 3 for the Friedmann equations of the dEGB cosmological model to calculate numerically the following quantity (see for example [82]):

$$\Omega(f, T_0)h^2 \equiv \frac{1}{\rho_{\text{crit}}(T_0)} \frac{d\rho_{\text{GW}}(T_0)}{d \ln f} h^2, \quad (5.6)$$

where $h = H_0/(100 \text{ km/s/Mpc})$ with H_0 the present value of the Hubble constant, $T_0 = 2.7 \text{ K}$ is the present CMB temperature, f the frequency measured today and $\rho_{\text{crit}} = 3H^2/(8\pi G)$ the critical density corresponding to a flat Universe. Note that the quantity $\Omega(f, T_0)h^2$ is independent of the actual Hubble expansion rate.

In order to calculate Eq. (5.6), we follow Refs. [67, 68] and proceed in two steps. First, we integrate Eq. (5.1) from some temperature T_{max} (that we will identify with the reheating temperature T_{RH} at the end of inflation) and $T_{\text{EWCO}} = 160 \text{ GeV}$ to obtain $d\rho_{\text{GW}}/d \ln k_{\text{EWCO}}$, where $k_{\text{EWCO}} = k(T) (g_{*s}(T_{\text{EWCO}})/g_{*s}(T))^{1/3} T_{\text{EWCO}}/T$ is the wave number at $T = T_{\text{EWCO}}$. In order to do this, in Eq. (5.1) we change variable from t to T by making use of Eq. (3.1). In a second step, we rescale the GW density from $T = T_{\text{EWCO}}$ to $T = T_0$ with the scale factor ratio $(a_{\text{EWCO}}/a_0)^4$ and we use

$$f = \frac{1}{2\pi} \left[\frac{g_{*s}(T_0)}{g_{*s}(T_{\text{EWCO}})} \right]^{\frac{1}{3}} \left(\frac{T_0}{T_{\text{EWCO}}} \right) k_{\text{EWCO}}, \quad (5.7)$$

to express the frequency f in terms of k_{EWCO} , and normalize the GW spectrum to the present photon density $\Omega_{\gamma,0} = 2.4729(21) \times 10^{-5}$ writing $h^2/\rho_{\text{crit}}(T_0) = 15/(\pi^2 T_0^4) \Omega_{\gamma,0}$. The final result is

$$\Omega_{\text{GW}}(f, T_0)h^2 = \Omega_{\gamma,0} h^2 \frac{\lambda}{M_{\text{PL}}} \int_{T_{\text{EWCO}}}^{T_{\text{Max}}} dT \left(\frac{g_{*0}}{g_{*s}(T)} \right)^{4/3} T^2 \hat{k}(f, T)^3 \frac{\eta(\hat{k}, T)}{\sqrt{\rho(T)}} \beta(T), \quad (5.8)$$

where $\Omega_{\text{GW}}(f, T_0)$ is the fraction of energy liberated into gravitational wave radiation per frequency octave [51, 83, 84], $\lambda = 30\sqrt{3}/\pi^4$, $\beta(T)$ is given by Eq. (3.2), $g_{*0} = 2$, $g_{*s}(T_0) = 3.91$, $g_{*s}(T_{\text{EWCO}}) = 106.75$, and

$$\hat{k}(f, T) = \left[\frac{g_{*s}(T)}{g_{*s}(T_0)} \right]^{\frac{1}{3}} \frac{2\pi f}{T_0}. \quad (5.9)$$

At production, the GW source term $\eta(\hat{k}, T)$ has a peak at $\hat{k} \simeq 3.92$ [68, 81] that is largely independent of the temperature, and whose position in the frequency f measured today corresponds to $f_{\text{peak}} \simeq 74 \text{ GHz}$, assuming the particle content of the Standard Model for $T > T_{\text{EWCO}}$.

5.1.2 Present and future stochastic GW observations

Presently, the only bound on the GW stochastic background discussed in the previous Section can be obtained from BBN, $\Omega(f, T_0)h^2 < 1.3 \times 10^{-6}$ [85]. In Figs. 10–12 this bound is represented by the horizontal solid line. We have also plotted a forecasted [86] future sensitivity (dotted line), $O(10^{-7})$, achievable with future satellite missions such as CORe [87] and EUCLID [88]. On the other hand, the current and planned sensitivity of GW experiments is far below the GHz frequency range, although some experimental ideas have the potential to reach it. For instance, an interesting possibility is the one proposed in [69] where gravitational waves can be observed by using the resonant quantum excitations of spin waves (magnons) produced inside a microwave cavity. However, the size of the cavity, $\simeq 5$ cm, is about one order of magnitude bigger than the one required to match the GW peak wavelength, and also its current sensitivity is not competitive with the BBN limit. Another interesting proposal is that of [70], where it has been suggested that GWs can be detected using resonant electromagnetic cavities. Currently, such detectors are only sensitive to frequencies below about 100 MHz. However, in [70] the projected sensitivity to the characteristic strain $h_c^2(f)$, which has an oscillatory behaviour in the frequency interval between 3.5×10^7 Hz and 10^9 Hz, seems to reach a plateau at higher frequencies that can potentially constrain the lower end of the stochastic GW background from the SM plasma. This can be seen in Figs. 10–12, where we have plotted the projected bound from [70] in the density vs frequency plane, showing the first resonant peak at around 3.5×10^7 Hz (solid line), and extrapolating the plateau up to 100 GHz (dashed line). In Figs. 10–12 we have converted the bound on $h_c^2(f)$ from Fig. 1 of [70] using $\Omega_{\text{GW}}(f) = (2\pi^2/3H_0^2)f^2 h_c^2(f)$ (see for example [89]). Indeed, below 10^9 Hz such constraint appears competitive to the BBN bound and potentially able to constrain the GB scenario. Of course, in order to obtain more robust bounds an extension of the experimental sensitivity to ~ 100 GHz will be required.

5.2 GW constraints from compact binary mergers

In this Section we summarize the bounds from the detection of Gravitational Waves from compact binary mergers and refer to Ref. [1] for further details.

Due to the Universe expansion even if $\dot{\phi}(T_{\text{BBN}}) \neq 0$ the evolution of the scalar field ϕ eventually freezes at some asymptotic temperature $T_L \ll T_{\text{BBN}}$ to a constant background value $\phi(T_L)$, implying no departure from GR at the cosmological level for $T < T_L$. On the other hand, in the vicinity of a BH or a NS the density profile of the scalar field is distorted compared to $\phi(T_L)$, leading to a local departure from GR that can modify the GW signal if the stellar object is involved in a merger event. Near the black hole or the neutron star the distortion of the scalar field is small and the dEGB function $f(\phi)$ can be expanded up to the linear term in the small perturbation $\Delta\phi$ around the asymptotic value $\phi(T_L)$ of the scalar field at large distance [56]

$$f(\phi) = f(\phi(T_L)) + f'(\phi(T_L))\Delta\phi + \mathcal{O}((\Delta\phi)^2). \quad (5.10)$$

In this way, the constraints from compact binary mergers is expressed in terms of $f'(\phi(T_L))$:

$$|f'(\phi(T_L))| \leq \sqrt{8\pi} \alpha_{\text{GB}}^{\text{max}}, \quad (5.11)$$

where we take $\alpha_{\text{GB}}^{\text{max}} = (1.18)^2 \text{ km}^2$ from the analysis of the LIGO-Virgo Collaboration data of Ref. [56]. The extra factor of $\sqrt{8\pi}$ in the equation above is due to the conversion from the units of Ref. [56] (that use $G = c = 1$) to those of the present work (where $\kappa = 8\pi G = c = 1$). Taking into account the residual evolution of ϕ from T_{BBN} to T_L when $\dot{\phi}(T_{\text{BBN}}) \neq 0$ [1] one obtains the final constraint:

$$\left| \tilde{\alpha} \gamma e^{\gamma \frac{\phi_{\text{BBN}}}{H_{\text{BBN}}}} \right| \leq \sqrt{8\pi} \alpha_{\text{GB}}^{\text{max}}. \quad (5.12)$$

5.3 Summary of GW bounds

Eq. (5.8) implies that the gravitational waves produced per e-fold scale as $d\Omega_{\text{GW}}/d \ln a \propto T^3/\sqrt{\rho}$. At the same time, since they are produced by the relativistic plasma, a sizeable density of GWs can only be produced when radiation is the dominant component of the energy density, i.e. when $\rho \propto T^4$. As a consequence, we conclude that, necessarily, $d\Omega_{\text{GW}}/d \ln a \propto T$, and that it is ultra-violet dominated, i.e. the integral of Eq (5.8) is driven by the contribution of the GWs emitted at high temperature [90]. In the case of a standard Cosmology, in which radiation is assumed to dominate the Universe expansion at all temperatures $T > T_{\text{EWCO}}$, this implies that the GW stochastic background is a monotonically growing function of T_{max} . This could potentially put bounds on the reheating temperature of the Universe T_{RH} , although for standard Cosmology the ensuing stochastic background turns out to be below the BBN bound even for values as high as $T_{\text{RH}} \simeq 10^{16}$ GeV [90]. On the other hand, for a non-standard cosmology where radiation dominance stops above some temperature $T_{\text{rad,max}}$ the stochastic background is dominated by the gravitational waves produced at $T_{\text{rad,max}}$, and increasing T_{max} beyond $T_{\text{rad,max}}$ does not change the final result, so that the prospects of detection are even worse than in standard Cosmology.

The dEGB scenario presents an interesting twist to the picture summarized above. In fact, as discussed in Sections 3 and 4, in sizeable parts of its parameter space one of the asymptotic solutions at high temperature corresponds to a “slow-roll regime” with $w = -1/3$ (see Section 4.3) where the energy density of the Universe is dominated by $\rho_{\text{rad}}, |\rho_{\text{GB}}| \propto T^4$ while at the same time $\rho_{\text{rad}} + \rho_{\text{GB}} \propto T^2$, with a large cancellation between ρ_{rad} and ρ_{GB} . As a consequence, this scenario has $d\Omega_{\text{GW}}/d \ln a \propto T^2$ and represents an exception to the argument summarized above according to which, necessarily, at most $d\Omega_{\text{GW}}/d \ln a \propto T$ during an epoch of sizeable GW production. This is due to the peculiar nature of dEGB, which allows to have an epoch when the relativistic plasma dominates the energy of the Universe while at the same time the rate of dilution with T of the total energy density is slower than what usually expected during radiation dominance⁹. As we will see this strongly enhances the GW expected signal compared to the standard case

⁹ ρ_{GB} is not a physical component of the energy density of the Universe, so the slow-roll regime is radiation-dominated in the sense that the plasma of relativistic particles is the only physical component of the energy-momentum tensor.

and allows to put sensible bounds on the reheating temperature $T_{\text{RH}} \lesssim 10^8 - 10^9 \text{ GeV} \ll 10^{16} \text{ GeV}$ in the regions of the dEGB parameter space corresponding to the “slow roll” asymptotic behaviour.

In light of the discussion above, we can expect an enhancement of the expected GW stochastic background in the regions of the parameter space where the “slow roll” asymptotic behaviour is achieved, i.e. in those regions that correspond to the flows ①, ② and ④ as indicated in Figs. 8 and 4.

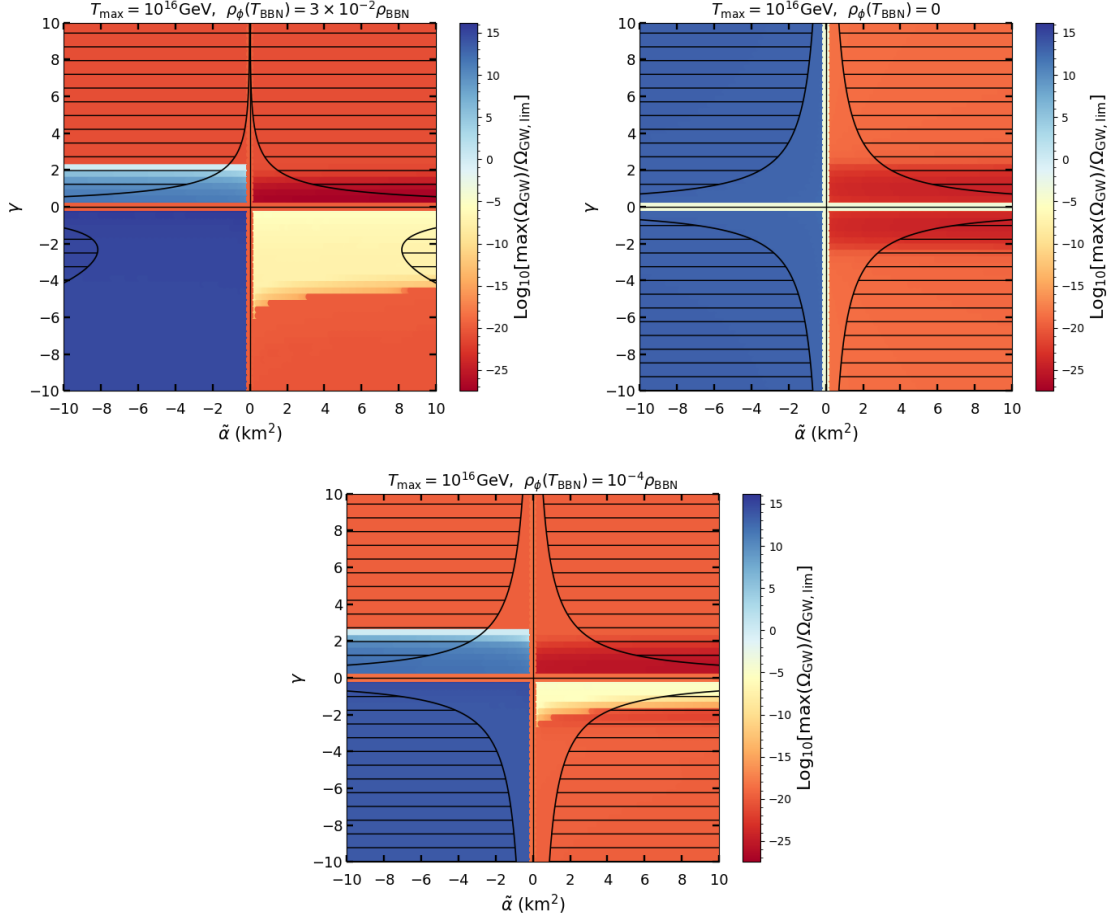


Figure 9. The color codes show the variations of the peak value of the GW stochastic background, normalised to the BBN upper limit ($\Omega_{\text{GW,lim}} h^2 \simeq 10^{-6}$), in the $\tilde{\alpha} - \gamma$ plane for different values of $\rho_{\phi}(T_{\text{BBN}})$: $3 \times 10^{-2} \rho_{\text{BBN}}$ (top left), 0 (top right) and $10^{-4} \rho_{\text{BBN}}$ (bottom). The maximum temperature of the Universe is assumed to be 10^{16} GeV . The hatched areas are ruled out by the detection of GW from compact binary mergers.

This is confirmed by the plots of Fig. 9, where the color code shows the peak value of the expected GW stochastic background for $T_{\text{max}} = 10^{16} \text{ GeV}$ normalised to the BBN upper limit. Specific examples of the expected GW stochastic frequency spectra for $\tilde{\alpha} = \pm 1 \text{ km}^2$, $\gamma = \pm 1$ and $\gamma = \pm 5$ (corresponding to each of the flows numbered from ① to ⑧ in Fig. 8) are also provided for reference in Fig. 10 ($\tilde{\alpha} > 0$) and 11 ($\tilde{\alpha} < 0$) in the case

when $T_{\text{max}} = 10^8$ GeV. The same figures also show the BBN bound and the prospective constraints (extrapolated to higher frequencies) from EM cavities of Ref. [70]. Indeed, the normalized GW peak value in Fig. 9 largely exceeds unity whenever the asymptotic equation of state corresponds to slow roll ($w = -1/3$), indicating that in such regions of the parameter space it is possible to set an upper bound on $T_{\text{max}} \ll 10^{16}$ GeV. This is confirmed by Fig. 15, where the cyan shaded areas for $\tilde{\alpha} < 0$ indicate the T_{max} bound obtained from the BBN constraint on the GW background, while the other regions (where the GW signals are too weak to obtain any bound) show the maximum possible temperature for the production of the GW signal (which corresponds to the highest temperature for which ρ_{rad} dominates the energy density of the Universe).

In particular, in agreement with the discussion of Section 4.4, a bound on T_{max} can be obtained for $\dot{\phi}(T_{\text{BBN}}) = 0$ in the full parameter space with $\tilde{\alpha} < 0$. However, for $\dot{\phi}(T_{\text{BBN}}) > 0$ the correspondence between the slow-roll regions in Fig. 4 and the high GW signal domains in Figs. 9 and 15 is no longer exact. Specifically, in Figs. 9 and 15 some regions with a high GW signal (or at least higher than in Standard Cosmology) are observed for configurations where $w \neq -1/3$. Moreover, at variance with the equation-of-state domains of Fig. 4, the regions of Fig. 9 show some dependence on the $\tilde{\alpha}$ parameter. The reason of such mismatch is simply because the GW production process depends on the whole expansion history of the Universe, and not only on its asymptotic behaviour at very large temperatures. In particular, as discussed in Section 4.4, for $\dot{\phi}(T_{\text{BBN}}) > 0$ there exist specific situations for which the boundary conditions at BBN imply $z_{\text{BBN}} > 0$ while the only available attractor is at $z < 0$ and is not slow-roll (instead, it is either kination at $(1, z \rightarrow 0^-)$ or $(x_{\text{fp}}, z_{\text{fp}})$). In such situations the boundary conditions at BBN “go against the flow”, and in order to cross the origin the system needs to follow the z axis with $w = -1/3$ for a while before eventually jumping to the real attractor at higher temperatures (see paths ⑥ and ⑧ in Fig. 8). In these cases a metastable regime is achieved where, although the asymptotic behaviour at high temperature is not slow-roll, the system does follow the slow-roll equation of state in some interval of temperatures, implying an enhancement of the GW signal compared to the case of standard Cosmology, albeit not at the same level of the cases when slow-roll is the stable attractor at indefinitely high T . This is the explanation of the region of intermediate values of the GW signal that is observed in Fig. 9 for $\dot{\phi}(T_{\text{BBN}}) > 0$, $\tilde{\alpha} > 0$ and $\gamma < 0$. The fact that such domain extends up to some maximal value of $|\gamma|$ can be explained in a qualitative way by noting that for $\gamma \rightarrow 0$ the attractor $(x_{\text{fp}}, z_{\text{fp}})$ moves away to $(+\infty, -\infty)$ along the $x + z = 1$ line, implying that for smaller values of $|\gamma|$ the corresponding flow (see path ⑧ in Fig. 8) detaches “later” from the z negative axis, and the metastable slow-roll solution responsible for the signal enhancement lasts longer. As a consequence for $\tilde{\alpha} < 0$ and $\gamma < 0$ the GW signal is a decreasing function of $|\gamma|$, as shown explicitly in Fig. 12.

To summarize the discussion of this Section, the stochastic GW background can set a meaningful bound on $T_{\text{max}} < 10^{16}$ GeV only for $\tilde{\alpha} < 0$, when the slow-roll attractor solution is achieved ($w = -1/3$). In particular when $\dot{\phi}(T_{\text{BBN}}) = 0$ the flow of the autonomous differential equations always moves from $(0, 0)$ directly toward $z < 0$ and the system quickly achieves the slow-roll asymptotic behaviour, so that such bound is possible for any value of γ . On the other hand when $\dot{\phi}(T_{\text{BBN}}) > 0$ the system originates from $(x_{\text{BBN}}, z_{\text{BBN}})$ with

$z_{\text{BBN}} \neq 0$. In this case, while for $\gamma < 0$ one has $z_{\text{BBN}} < 0$, and a situation similar to the $\dot{\phi}(T_{\text{BBN}}) = 0$ case is obtained, when $\gamma > 0$ one has $z_{\text{BBN}} > 0$. In this case when $\gamma < \sqrt{6\kappa}$ slow roll remains the only attractor, so that the system eventually reaches it after crossing the origin. However, when $\gamma > \sqrt{6\kappa}$ a second attractor appears at $(1, z \rightarrow 0^+)$ which deviates the flow away from slow-roll toward kination. As a consequence, for $\gamma \gtrsim \sqrt{6\kappa}$ the expected GW stochastic background is suppressed and no bound on T_{max} can be obtained. Explicit examples of the bounds on T_{max} that can be obtained for $\tilde{\alpha} < 0$ are represented by the curves in Fig. 14, where $\tilde{\alpha} = -1 \text{ km}^2$. In such Figure the dashed blue line shows that a bound of order $T_{\text{max}} \lesssim 10^9 \text{ GeV}$ can be obtained at all γ values when $\rho_\phi(T_{\text{BBN}}) = 0$, while for $\rho_\phi(T_{\text{BBN}}) = 3 \times 10^{-2} \rho_{\text{BBN}}$ (red solid line) and $\rho_\phi(T_{\text{BBN}}) = 10^{-4} \rho_{\text{BBN}}$ (green dashed line) the bounds quickly disappear for $\gamma \gtrsim \sqrt{6\kappa}$.

In figures 9 and 15 the shaded regions are combined with hatched areas ruled out by the merger events discussed in Section 5.2 and obtained using Eq. (5.12). From such figures one can notice that the GW bound from binaries allows to constrain the dEGB parameter space in some of the regions ($\tilde{\alpha} > 0$ and $\tilde{\alpha} < 0$, $\gamma > \sqrt{6\kappa}$) where the high-temperature asymptotic equation of state does not correspond to slow roll ($w = -1/3$) and the GW stochastic background is suppressed. Moreover, such bound does not depend on T_{RH} . The complementarity between the two bounds is also observed for $\tilde{\alpha} < 0$ and $\gamma > 0$, where the bound from the GW stochastic background relaxes quickly as $\gamma \rightarrow \sqrt{6\kappa}$ (see Fig. 14).

6 Conclusions

In spite of a high degree of non linearity and phenomenological complexity at low temperature, Cosmology in the dilaton-Einstein-Gauss-Bonnet (dEGB) scenario of modified gravity exhibits only very few asymptotic behaviours at large temperature, characterized by only a few values of the equation of state $w = p/\rho$ (with ρ and p the energy density and pressure of the Universe, respectively), when the model is required to reproduce Standard Cosmology at BBN. In the present paper we have provided a transparent and systematic discussion of such high temperature asymptotic behaviours, that were first observed in the numerical analysis of Ref. [1].

By re-expressing the Friedmann equations of the model (Eqs.(2.4, 2.5, 2.6)) in terms of a set of autonomous differential equations (Eqs. (4.8, 4.9)) we found that the such asymptotic behaviours have a clear interpretation in terms of a pattern of attractors (see Table 1 and Fig. 8). Specifically, in terms of the dEGB parameters $\tilde{\alpha}$ and γ and of the value of the kinetic energy of the scalar field at BBN $\rho_\phi(T_{\text{BBN}})$, we found that:

- The model presents only three attractors at high temperature : slow-roll ($w = -1/3$), kination ($w = 1$) and fast-roll ($1 < w < 7/3$).
- The way such attractor solutions are approached depends on only three conditions: (i) $\tilde{\alpha} > 0$ or $\tilde{\alpha} < 0$; (ii) $\gamma > 0$ or $\gamma < 0$; (iii) $|\gamma| < \sqrt{6\kappa}$ or $|\gamma| > \sqrt{6\kappa}$. The combination of these three dichotomies generates eight possible paths for the evolution of the system at high temperature, represented in Fig. 8 and in Table 1 with the numbers from ① to ⑧. When $\rho_\phi(T_{\text{BBN}}) = 0$ only half of the paths are followed: ②, ④,

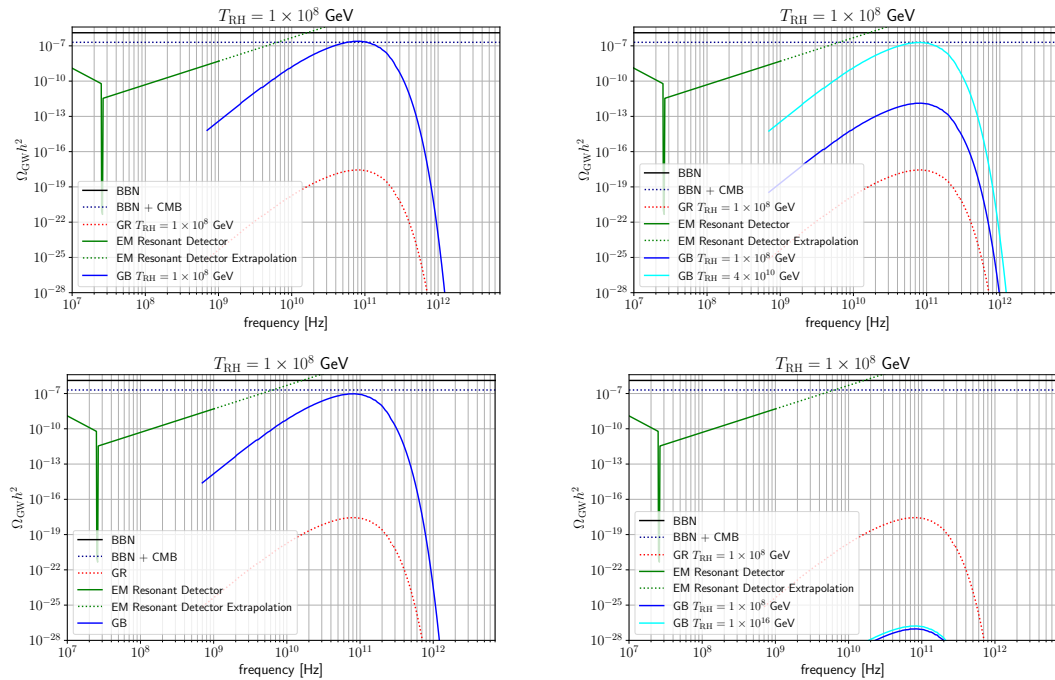


Figure 10. Gravitational Wave density, $\Omega_{\text{GW}} h^2$, as a function of the frequency, for several dEGB models. The solid line is the current BBN limit [85] while the dotted line is a forecasted sensitivity from the future CORe and EUCLID satellite missions [86]. The solid green line corresponds to the resonant detector bound projection of [70], extrapolated to higher frequencies by the dotted line (see Section 5.1.2). In all plots $\tilde{\alpha} = -1 \text{ km}^2$. First panel: $\gamma = -1$, second panel: $\gamma = 1$, third panel $\gamma = -5$, fourth panel $\gamma = 5$.

⑤ and ⑦). For our conventional choice $\dot{\phi}(T_{\text{BBN}}) > 0$ such paths are also followed when $\rho_\phi(T_{\text{BBN}}) \neq 0$ if $\tilde{\alpha}\gamma < 0$, leading to phenomenological results very similar to the corresponding ones for $\dot{\phi}(T_{\text{BBN}}) = 0$.

- The correspondence between path and asymptotic w is the following: $w = -1/3$ (slow-roll) for ①, ② and ④; $w = 1$ (kination) for ③, ⑦ and ⑧; $1 < w < 7/3$ (fast-roll) for ⑤ and ⑥).
- The effect of the GB term on the evolution of the Friedmann equations can be parameterized in term of the additional component ρ_{GB} to the energy density of the Universe (see Eq. (2.4)). Such component is not physical, since it can be negative. Paths ①, ⑥ and ⑧ are characterized by the fact that the boundary conditions imply $\rho_{\text{GB}}(T_{\text{BBN}}) > 0$, while the only available attractor at high temperature has $\rho_{\text{GB}} < 0$. This requires a change in the sign of ρ_{GB} and, so of $\dot{\phi}$, that makes the approaching path to the attractor longer (the system need to “go against the flow”, see discussion in Section 5.3). Such cases, which are only possible for $\dot{\phi}(T_{\text{BBN}}) \neq 0$, are characterized by the emergence of meta-stable solutions, where the system follows an equation of state for a while at intermediate temperatures before eventually jumping to the real attractor at higher temperatures. Specifically, for ① the system follows kination

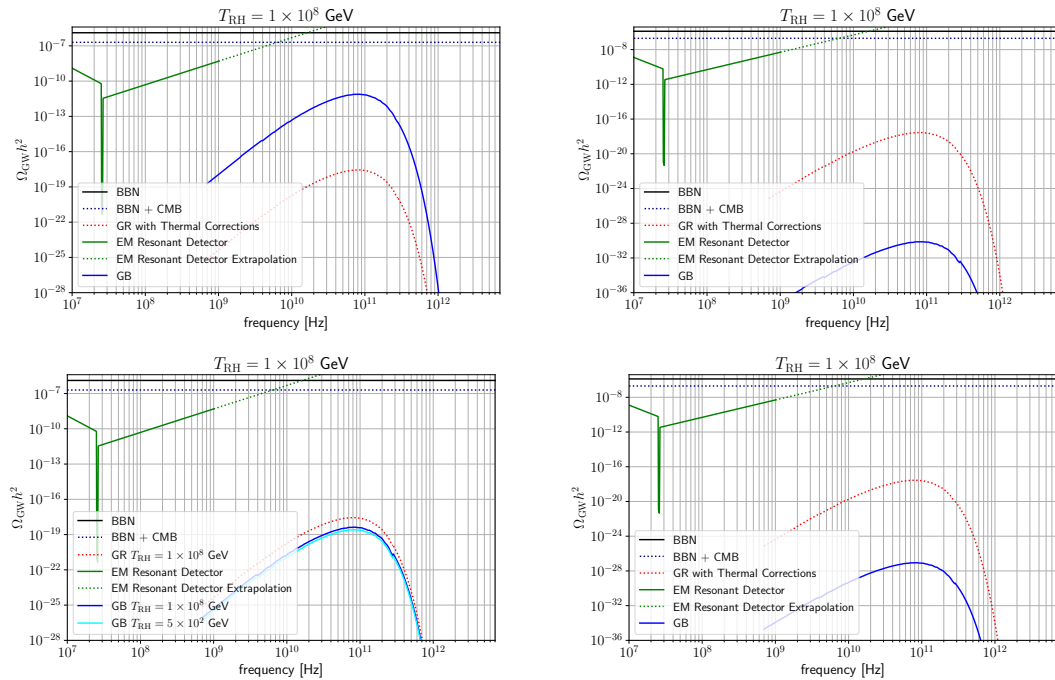


Figure 11. Same as Fig. 10, but for all of these cases $\tilde{\alpha} = 1 \text{ km}^2$. For the first panel $\gamma = -1$, second panel $\gamma = 1$, third panel $\gamma = -5$ and fourth panel $\gamma = 5$.

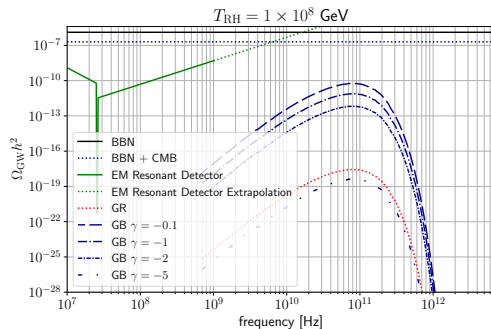


Figure 12. Same as in Figs. (10-11) for $\tilde{\alpha} = 1 \text{ km}^2$ and different values of $\gamma < 0$. The signal is enhanced as $|\gamma| \rightarrow 0$ because the metastable slow-roll solution with $w = -1/3$ lasts longer (see Fig. 13).

($w = 1$) before jumping to slow-roll ($w = -1/3$), while for ⑥ and ⑧ the system follows slow-roll ($w = -1/3$) before jumping to fast roll ($1 < w < 7/3$). We notice that in the analysis of Ref. [1] the evolution of the dEGB Friedmann equations was limited to the temperatures relevant for WIMP thermal decoupling, and the case $\tilde{\alpha} = 1 \text{ km}^2$, $\gamma = 1$, $\rho_\phi(T_{\text{BBN}}) = 3 \times 10^{-2} \rho_{\text{BBN}}$ (corresponding to the path ⑥) was mistakenly assumed to have the slow-roll asymptotic behaviour, missing the transition to fast roll at higher temperatures.

- Compared to standard Cosmology, the regions of the dEGB parameter space cor-

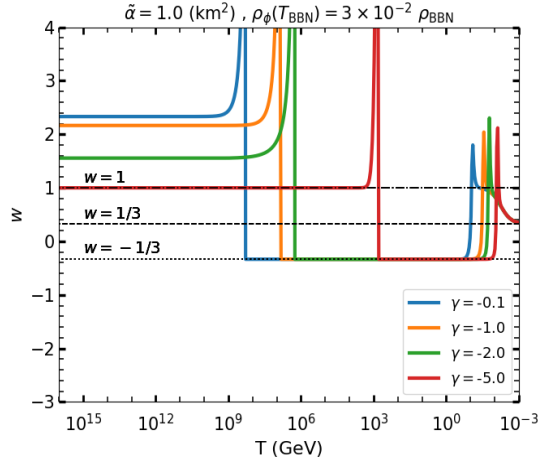


Figure 13. Evolution of the equation of state for $\tilde{\alpha} = +1 \text{ km}^2$, $\rho_\phi(T_{\text{BBN}}) = 3 \times 10^{-2} \rho_{\text{BBN}}$, for different negative values of γ . As $|\gamma| \rightarrow 0$ the system follows the metastable solution $w = -1/3$ for a larger interval of temperatures before jumping to a different regime, implying an increasing GW stochastic background (see Fig. 12).

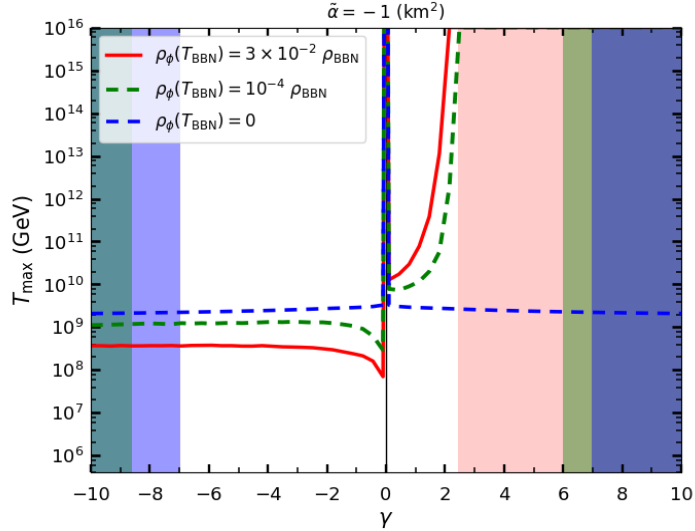


Figure 14. GW upper bounds on the maximum temperature of the Universe as a function of γ and for $\tilde{\alpha} = -1 \text{ km}^2$. In the caption $\kappa = 1$. The curves represent the bounds obtained by imposing that the peak value of the GW stochastic background does not exceed the BBN upper limit ($\Omega_{\text{GW,lim}} h^2 \simeq 10^{-6}$), while the shaded areas are excluded by the observation of GW from binary mergers. The red, green and blue curve and shaded areas correspond to $\rho_\phi(T_{\text{BBN}}) = 3 \times 10^{-2} \rho_{\text{BBN}}$, $10^{-4} \rho_{\text{BBN}}$ and 0, respectively.

responding to a slow-roll asymptotic equation of state ($w = -1/3$) imply a strong enhancement of the expected Gravitational Wave stochastic background produced by the primordial plasma of relativistic particles. This already allows to use the bound from BBN to put sensible bounds on $T_{\text{RH}} \simeq 10^8 - 10^9 \text{ GeV} \ll 10^{16} \text{ GeV}$. Interestingly,

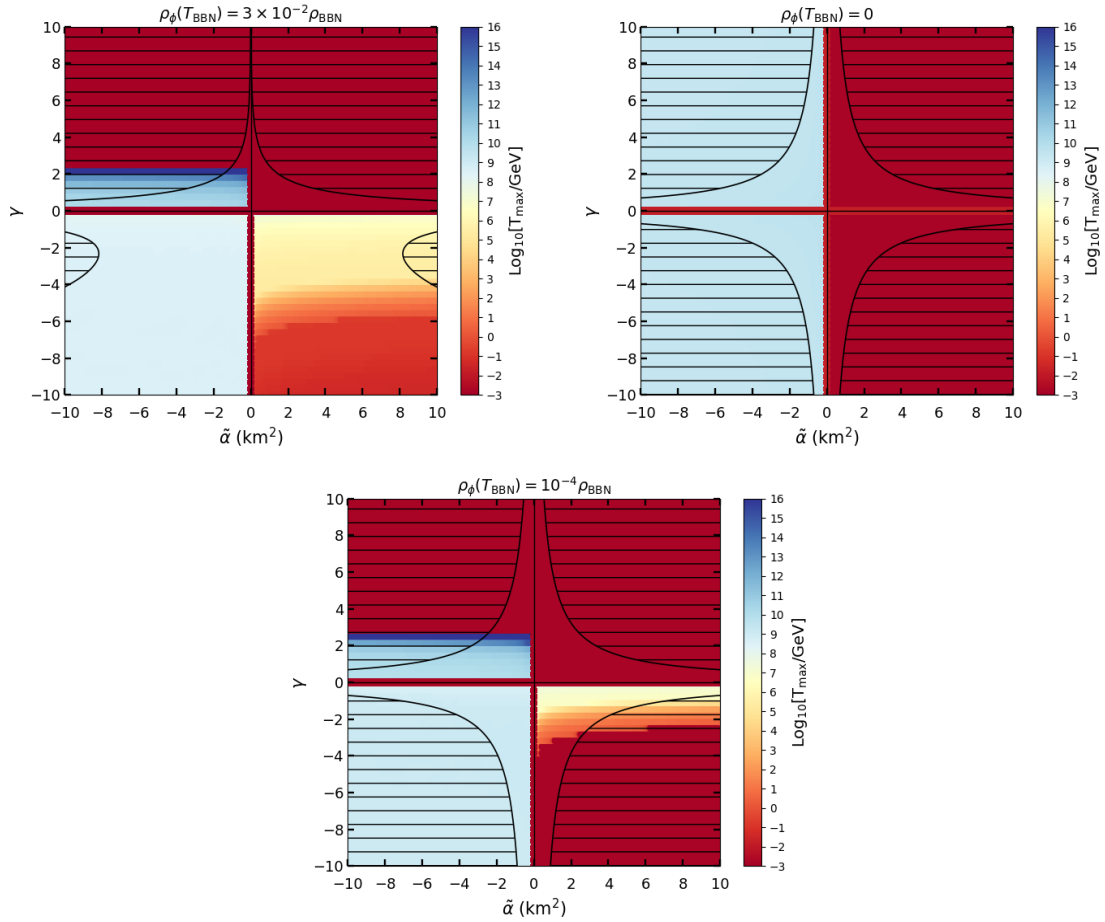


Figure 15. The color codes show the variations of T_{\max} in the $\tilde{\alpha} - \gamma$ plane for different values of $\rho_\phi(T_{\text{BBN}})$: $3 \times 10^{-2} \rho_{\text{BBN}}$ (top left), 0 (top right) and $10^{-4} \rho_{\text{BBN}}$ (bottom). In each plot, the cyan region for $\tilde{\alpha} < 0$ indicates the upper bound on the maximum temperature of the Universe obtained from the BBN constraint on GW background, while the other regions (where the GW signals are too weak to obtain any bound) show the maximum possible temperature for the production of the GW signal. The hatched areas are ruled out by the detection of GW from compact binary mergers.

such enhancement is possible because slow-roll in dEGB allows to have an epoch when the energy density ρ_{rad} of the relativistic plasma dominates the energy of the Universe while at the same time the rate of dilution with T of the total energy density is slower than what usually expected during radiation dominance (specifically, the energy density of the Universe is dominated by ρ_{rad} , $|\rho_{\text{GB}}| \propto T^4$ while at the same time $\rho_{\text{rad}} + \rho_{\text{GB}} \propto T^2$, with a large cancellation between ρ_{rad} and ρ_{GB}).

- The GW bound from binaries allows to constrain the dEGB parameter space in some of the regions where the high-temperature asymptotic equation of state does not correspond to slow roll ($w = -1/3$) and the GW stochastic background is suppressed. Moreover, such bound does not depend on T_{RH} .

We conclude by pointing out that we analyzed dEGB cosmology by fixing the boundary

conditions of the Friedmann equations at BBN and run them to higher temperatures, i.e. backward in time. On the other hand, the physical (causal) evolution of the Universe is obtained by reversing the flow, starting from some initial conditions at high temperatures. In such case the origin of the $x-z$ plane, which corresponds to standard radiation dominated Λ CDM Cosmology, is technically not a critical point of the set of autonomous equations (4.8, 4.9). Indeed, the flow can cross the origin (see for instance the paths ①, ③, ⑥ and ⑧ of Fig. 8) so that $x', z' \neq 0$ for $(x, z) = (0, 0)$. Nevertheless, when the Friedmann equations are run below BBN one observes that both ρ_{GB} and V'_{GB} are suppressed by their dependence on H , while the friction term in the scalar field equation (2.6) eventually drives $\dot{\phi}$ to zero. This implies that, starting from some high temperature T_{max} , when the system is evolved for a large-enough number ΔN of e-foldings it eventually gets arbitrarily close to the origin at lower temperatures (without formally reaching it) and Standard Cosmology is recovered. From this perspective the BBN bound rules out high-temperature configurations for which ΔN is too large, and Standard Cosmology is achieved too late (specifically, below T_{BBN}). By fixing the boundary conditions at BBN the high-temperature solutions found in the present paper reach standard Cosmology fast enough by construction, but one may wonder if they require some level of fine tuning i.e. if ΔN is sensitive to them. A discussion of this aspect would require a dedicated and systematic numerical exploration of the Friedmann equations that goes beyond the scope of the present paper. It would be an important aspect to consider when discussing which inflationary and reheating models within dEGB can lead to Cosmologies compatible to observation.

Acknowledgements

This research was supported by the National Research Foundation of Korea (NRF) funded by the Ministry of Education through the Center for Quantum Space Time (CQUeST) with grant number 2020R1A6A1A03047877 and by the Ministry of Science and ICT with grant numbers RS-2023-00241757. The work of H.C. Lee and L. Velasco-Sevilla is partially supported by the National Research Foundation of Korea (NRF) grant, RS-2023-00273508, B.-H. Lee (2020R1F1A1075472) and W. Lee (2022R1I1A1A01067336). BHL thanks APCTP and KIAS, where part of this work was done, for the warm hospitality. L. Yin is supported by an appointment to the YST Program at the APCTP through the Science and Technology Promotion Fund and Lottery Fund of the Korean Government.

A Thermal corrections

In order to identify with ease the thermal corrections computed in [68], we collect the expressions of [67] and [68] rewritten in [81] with different notation. The function $\eta(T, \hat{k})$ can be identified with $R(T, \hat{k})$, from Eq. (6.5) of [67] and Γ from [68] as follows:

$$R(\hat{k}, T) = 2k\Gamma n_B(\hat{k}) = 32\pi \frac{T^4}{M_{\text{PL}}^2} \eta(\hat{k}, T), \quad (\text{A.1})$$

where the function Γ is the main subject of computation in [68]. Hence $\eta(T, \hat{k})$ is given by

$$\eta(\hat{k}, T) = \frac{1}{16\pi} \frac{k}{T^4} M_{PL}^2 \Gamma n_B(\hat{k}). \quad (\text{A.2})$$

We write the contributions to Γ with the same notation used in Eq. (2.8) of [68] for the Euclidean correlator $G_{12;12}^E$ as

$$\Gamma(k) = \frac{16\pi \text{Im} (G_{12;12}^E|_{k_n \rightarrow -i[k+i0^+]})}{k M_{PL}^2}, \quad (\text{A.3})$$

where $G_{12;12}^E$ is a function of the 1-loop diagrams and 2-loop diagrams (for which for example $\Phi_{a(b)}$ represents the 2-loop diagram describing the coupling of the particle of type a to $T_{\mu\nu}$ where a particle of type b appears in the loop). Hence we write

$$\text{Im} (G_{12;12}^E|_{k_n \rightarrow -i[k+i0^+]}) = \sum C_{\Phi_x} \hat{\Phi}_x, \quad (\text{A.4})$$

where C_{Φ_x} is a numerical coefficient and $\hat{\Phi}_x$ is a loop function. Both can be read off from Eq. (2.6) of [68] after taking the limit of Eq. (A.4). In this way, we can identify all the components of $\eta(\hat{k}, T)$ of Eq. (5.3) and Eq. (5.5) since then, Eq. (A.2) becomes

$$\eta(\hat{k}, T) = \frac{n_B(\hat{k})}{T^4} \sum C_{\Phi_x} \hat{\Phi}_x. \quad (\text{A.5})$$

Taking $D = 4$, $N_g = 3$ in Eq. (2.8) of [68], we have

$$\eta_{\text{HTL}}(\hat{k}, T) = \frac{n_B(\hat{k})}{T^4} \frac{1}{4} \sum_{i=1,2,3} (2 + N_c^i C_F^i) \hat{\Phi}_g^i, \quad (\text{A.6})$$

where $i = 1, 2, 3$ runs over the SM gauge factors $C_F = (N_c^2 - 1)/2N_c$, N_c being of course different for the different SM gauge groups, and

$$\begin{aligned} \eta^T(\hat{k}, T) = & \frac{1}{4} \frac{n_B(\hat{k})}{T^4} \left\{ [(3g_2^2 + 12g_3^2)] \hat{\Phi}_{g(g)} + (g_1^2 + 3g_2^2) [\hat{\Phi}_{s(g)} + \hat{\Phi}_{g(s)} + \hat{\Phi}_{s|g}] \right. \\ & + (5g_1^2 + 9g_2^2 + 24g_3^2) [\hat{\Phi}_{f(g)} + \hat{\Phi}_{g(f)} + \hat{\Phi}_{f|g}] \\ & \left. + (3|y_t|^2 + 3|y_b|^2 + |y_\tau|^2) [\hat{\Phi}_{s(f)} + \hat{\Phi}_{f(s)} + \hat{\Phi}_{s|f}] \right\}. \end{aligned} \quad (\text{A.7})$$

Therefore, we can identify the functions $\eta_{gg}(\hat{k})$, $\eta_{sg}(\hat{k})$, $\eta_{fg}(\hat{k})$ and $\eta_{sf}(\hat{k})$, for example

$$\eta_{gg}(\hat{k}) = \frac{1}{4} \frac{n_B(\hat{k})}{T^4} [\hat{\Phi}_{s(g)} + \hat{\Phi}_{g(s)} + \hat{\Phi}_{s|g}]. \quad (\text{A.8})$$

The important point is that all of the functions $\eta_{gg}(\hat{k})$ and of course equivalently $\hat{\Phi}$ have contributions from t and s channels. In this way, we can write

$$[\hat{\Phi}_{s(g)} + \hat{\Phi}_{g(s)} + \hat{\Phi}_{s|g}] = H_+^t + H_+^s, \quad (\text{A.9})$$

where the functions H_+^t and H_+^s can be read off from Eqs. (2.60), (2.61), (2.71) with the coefficients of Eqs. (2.72-2.75) of [68]. Hence, we get for all of the functions appearing in Eq. (A.7) the following expressions:

$$\begin{aligned}
\eta_{gg}(\hat{k}) &= \frac{1}{4} \frac{n_B(\hat{k})}{T^4} \left(H_+^t(\hat{k}) + H_+^s(\hat{k}) \right), \\
\eta_{sg}(\hat{k}) &= \frac{1}{4} \frac{n_B(\hat{k})}{T^4} \left[\frac{1}{4} \left(H_+^t(\hat{k}) + H_+^s(\hat{k}) \right) \right], \\
\eta_{sf}(\hat{k}) &= \frac{1}{4} \frac{n_B(\hat{k})}{T^4} \left[K^t(\hat{k}) + K^s(\hat{k}) \right], \\
\eta_{fg}(\hat{k}) &= \frac{1}{4} \frac{n_B(\hat{k})}{T^4} \left[-H_-^t - H_-^s \right],
\end{aligned} \tag{A.10}$$

where in the notation of [81], this translates into

$$\begin{aligned}
H_\pm^t(\hat{k}) &= \frac{\mathcal{I}_\pm(\hat{k}) T^4}{-16n_B(\hat{k})}, \quad H_\pm^s(\hat{k}) = \frac{\mathcal{J}_\pm(\hat{k}) T^4}{-16n_B(\hat{k})}, \\
K^t(\hat{k}) &= \frac{\mathcal{K}(\hat{k}) T^4}{16n_B(\hat{k})}, \quad K^s(\hat{k}) = \frac{\mathcal{L}(\hat{k}) T^4}{16n_B(\hat{k})},
\end{aligned} \tag{A.11}$$

and hence

$$\begin{aligned}
H_\pm^t(\hat{k}) &= \frac{4T^4}{(4\pi)^3 \hat{k}} \int_{-\infty}^{\hat{k}} dx \int_{|x|}^{2\hat{k}-x} dy \left[(1 + n_B(x) + n_B(\hat{k} - x))(y^2 - x^2) \right. \\
&\quad \left. - \frac{2}{3} L_1^\pm + \frac{(y^2 - 3(x - 2\hat{k})^2)(12L_3^\pm + 6yL_2^\pm + y^2L_1^\pm)}{6y^4} \right. \\
&\quad \left. + \frac{(1 \pm 3)x\hat{k}^2\pi^2}{y^4} (y^2 - x^2) \right].
\end{aligned} \tag{A.12}$$

Here, we note the missing “ x ” factor in Eq. (A.2) of [81], which we include here in the last line of Eq. (A.12). This factor simply follows from Eq. (2.61) of [68], coming from the divergent part of the t-channel contribution. The functions L_i^\pm are given in Eqs. (A.4) of [81] and can be identified with Eqs. (2.57-2.59) of [68] with the appropriate coefficients given in Eqs. (2.72-2.75) of [68]. For the s-channel contribution we have

$$\begin{aligned}
H_\pm^s(\hat{k}) &= \frac{4T^4}{(4\pi)^3 \hat{k}} \int_{\hat{k}}^{\infty} dx \int_{|2\hat{k}-x|}^x dy (n_B(x - \hat{k}) - n_B(x))(y^2 - x^2) \left(\frac{1}{3} (2M_1^\pm(x, y) - y) \right. \\
&\quad \left. - \frac{(y^2 - 3(x - 2\hat{k})^2)}{6y^4} (12M_3^\pm(x, y) + 6yM_2^\pm(x, y) + y^2M_1^\pm(x, y)) \right. \\
&\quad \left. + (x - 2\hat{k}) \left[\hat{M}_2^\pm(x, y) - 2y\hat{M}_1^\pm(x, y) \right] \right),
\end{aligned} \tag{A.13}$$

where $x = q_0/T$, $y = q/T$, q_0 and q the quantities (momenta) appearing in Eq. (2.71)[68] $\hat{M}_2^+ = \frac{2}{T^2}(\hat{L}_2^- - \hat{L}_2^+) = 0$ and $\hat{M}_1^+ = \frac{2}{T}(\hat{L}_1^- - \hat{L}_1^+) = 0$. The functions M_i^\pm are given in Eq. (A.4) of [81] and can be extracted from Eqs. (2.68-2.70) with the appropriate coefficients of Eqs. (2.72-2.75) of [68]. For the functions \mathcal{K} and \mathcal{L} we find expressions in agreement with those in Eq. (A.2) of [81].

References

- [1] A. Biswas, A. Kar, B.-H. Lee, H. Lee, W. Lee, S. Scopel et al., *WIMPs in dilatonic Einstein Gauss-Bonnet cosmology*, *JCAP* **08** (2023) 024, [[2303.05813](#)].
- [2] J.-c. Hwang and H. Noh, *Conserved cosmological structures in the one loop superstring effective action*, *Phys. Rev. D* **61** (2000) 043511, [[astro-ph/9909480](#)].
- [3] M. Satoh and J. Soda, *Higher Curvature Corrections to Primordial Fluctuations in Slow-roll Inflation*, *JCAP* **09** (2008) 019, [[0806.4594](#)].
- [4] G. W. Horndeski, *Second-order scalar-tensor field equations in a four-dimensional space*, *Int. J. Theor. Phys.* **10** (1974) 363–384.
- [5] R. P. Woodard, *Ostrogradsky’s theorem on Hamiltonian instability*, *Scholarpedia* **10** (2015) 32243, [[1506.02210](#)].
- [6] D. G. Boulware and S. Deser, *String Generated Gravity Models*, *Phys. Rev. Lett.* **55** (1985) 2656.
- [7] B. Zwiebach, *Curvature Squared Terms and String Theories*, *Phys. Lett. B* **156** (1985) 315–317.
- [8] R.-G. Cai, *Gauss-Bonnet black holes in AdS spaces*, *Phys. Rev. D* **65** (2002) 084014, [[hep-th/0109133](#)].
- [9] S. Nojiri and S. D. Odintsov, *Introduction to modified gravity and gravitational alternative for dark energy*, *eConf* **C0602061** (2006) 06, [[hep-th/0601213](#)].
- [10] S. Nojiri and S. D. Odintsov, *Unified cosmic history in modified gravity: from $F(R)$ theory to Lorentz non-invariant models*, *Phys. Rept.* **505** (2011) 59–144, [[1011.0544](#)].
- [11] T. Clifton, P. G. Ferreira, A. Padilla and C. Skordis, *Modified Gravity and Cosmology*, *Phys. Rept.* **513** (2012) 1–189, [[1106.2476](#)].
- [12] T. Harko, F. S. N. Lobo and M. K. Mak, *Arbitrary scalar field and quintessence cosmological models*, *Eur. Phys. J. C* **74** (2014) 2784, [[1310.7167](#)].
- [13] S. Bahamonde, C. G. Böhmmer, S. Carloni, E. J. Copeland, W. Fang and N. Tamanini, *Dynamical systems applied to cosmology: dark energy and modified gravity*, *Phys. Rept.* **775-777** (2018) 1–122, [[1712.03107](#)].
- [14] S. D. Odintsov and V. K. Oikonomou, *The reconstruction of $f(\phi)R$ and mimetic gravity from viable slow-roll inflation*, *Nucl. Phys. B* **929** (2018) 79–112, [[1801.10529](#)].
- [15] S. Alexander and E. McDonough, *Axion-Dilaton Destabilization and the Hubble Tension*, *Phys. Lett. B* **797** (2019) 134830, [[1904.08912](#)].
- [16] A. Banerjee, H. Cai, L. Heisenberg, E. O. Colgáin, M. M. Sheikh-Jabbari and T. Yang, *Hubble sinks in the low-redshift swampland*, *Phys. Rev. D* **103** (2021) L081305, [[2006.00244](#)].
- [17] Z.-K. Guo and D. J. Schwarz, *Slow-roll inflation with a Gauss-Bonnet correction*, *Phys. Rev. D* **81** (2010) 123520, [[1001.1897](#)].
- [18] S. Koh, B.-H. Lee, W. Lee and G. Tumurtushaa, *Observational constraints on slow-roll inflation coupled to a Gauss-Bonnet term*, *Phys. Rev. D* **90** (2014) 063527, [[1404.6096](#)].
- [19] S. Koh, *Cosmological Dynamics of a Scalar Field with Gauss-Bonnet Corrections*, *New Phys. Sae Mulli* **64** (2014) 1223–1228.

- [20] S. Lahiri, *Anisotropic inflation in Gauss-Bonnet gravity*, *JCAP* **09** (2016) 025, [[1605.09247](#)].
- [21] I. V. Fomin and S. V. Chervon, *Exact inflation in Einstein–Gauss–Bonnet gravity*, *Grav. Cosmol.* **23** (2017) 367–374, [[1704.03634](#)].
- [22] Z. Yi, Y. Gong and M. Sabir, *Inflation with Gauss-Bonnet coupling*, *Phys. Rev. D* **98** (2018) 083521, [[1804.09116](#)].
- [23] S. D. Odintsov and V. K. Oikonomou, *Viable Inflation in Scalar-Gauss-Bonnet Gravity and Reconstruction from Observational Indices*, *Phys. Rev. D* **98** (2018) 044039, [[1808.05045](#)].
- [24] E. O. Pozdeeva, M. R. Gangopadhyay, M. Sami, A. V. Toporensky and S. Y. Vernov, *Inflation with a quartic potential in the framework of Einstein-Gauss-Bonnet gravity*, *Phys. Rev. D* **102** (2020) 043525, [[2006.08027](#)].
- [25] S. Kawai and J. Kim, *Primordial black holes from Gauss-Bonnet-corrected single field inflation*, *Phys. Rev. D* **104** (2021) 083545, [[2108.01340](#)].
- [26] S. Nojiri and S. D. Odintsov, *Propagation speed of gravitational wave in scalar–Einstein–Gauss-Bonnet gravity*, *Nucl. Phys. B* **998** (2024) 116423, [[2308.06731](#)].
- [27] S. Kawai and J. Kim, *Probing the inflationary moduli space with gravitational waves*, *Phys. Rev. D* **108** (2023) 103537, [[2308.13272](#)].
- [28] C. van de Bruck, K. Dimopoulos and C. Longden, *Reheating in Gauss-Bonnet-coupled inflation*, *Phys. Rev. D* **94** (2016) 023506, [[1605.06350](#)].
- [29] S. Koh, B.-H. Lee and G. Tumurtushaa, *Constraints on the reheating parameters after Gauss-Bonnet inflation from primordial gravitational waves*, *Phys. Rev. D* **98** (2018) 103511, [[1807.04424](#)].
- [30] N. Rashidi and K. Nozari, *Gauss-Bonnet Inflation after Planck2018*, *Astrophys. J.* **890** (1, 2020) 58, [[2001.07012](#)].
- [31] V. K. Oikonomou, P. Tsyba and O. Razina, *Einstein–Gauss–Bonnet cosmological theories at reheating and at the end of the inflationary era*, *Annals Phys.* **462** (2024) 169597, [[2401.11273](#)].
- [32] S. Nojiri, S. D. Odintsov and M. Sasaki, *Gauss-Bonnet dark energy*, *Phys. Rev. D* **71** (2005) 123509, [[hep-th/0504052](#)].
- [33] G. Cognola, E. Elizalde, S. Nojiri, S. Odintsov and S. Zerbini, *String-inspired Gauss-Bonnet gravity reconstructed from the universe expansion history and yielding the transition from matter dominance to dark energy*, *Phys. Rev. D* **75** (2007) 086002, [[hep-th/0611198](#)].
- [34] S. Nojiri, S. D. Odintsov and D. Sáez-Chillón Gómez, *Unifying inflation with early and late dark energy in Einstein–Gauss–Bonnet gravity*, *Phys. Dark Univ.* **41** (2023) 101238, [[2304.08255](#)].
- [35] H. Mohseni Sadjadi, *Non-minimally coupled quintessence in the Gauss-Bonnet model, symmetry breaking, and cosmic acceleration*, [2310.03697](#).
- [36] J. J. Terente Díaz, K. Dimopoulos, M. Karčiauskas and A. Racioppi, *Gauss-Bonnet Dark Energy and the speed of gravitational waves*, *JCAP* **10** (2023) 031, [[2307.06163](#)].
- [37] P. Kanti, N. E. Mavromatos, J. Rizos, K. Tamvakis and E. Winstanley, *Dilatonic black holes in higher curvature string gravity*, *Phys. Rev. D* **54** (1996) 5049–5058, [[hep-th/9511071](#)].

- [38] Z.-K. Guo, N. Ohta and T. Torii, *Black Holes in the Dilatonic Einstein-Gauss-Bonnet Theory in Various Dimensions. I. Asymptotically Flat Black Holes*, *Prog. Theor. Phys.* **120** (2008) 581–607, [[0806.2481](#)].
- [39] W.-K. Ahn, B. Gwak, B.-H. Lee and W. Lee, *Instability of Black Holes with a Gauss–Bonnet Term*, *Eur. Phys. J. C* **75** (2015) 372, [[1412.4189](#)].
- [40] S. Khimphun, B.-H. Lee and W. Lee, *Phase transition for black holes in dilatonic Einstein-Gauss-Bonnet theory of gravitation*, *Phys. Rev. D* **94** (2016) 104067, [[1605.07377](#)].
- [41] G. Antoniou, A. Bakopoulos and P. Kanti, *Evasion of No-Hair Theorems and Novel Black-Hole Solutions in Gauss-Bonnet Theories*, *Phys. Rev. Lett.* **120** (2018) 131102, [[1711.03390](#)].
- [42] D. D. Doneva and S. S. Yazadjiev, *New Gauss-Bonnet Black Holes with Curvature-Induced Scalarization in Extended Scalar-Tensor Theories*, *Phys. Rev. Lett.* **120** (2018) 131103, [[1711.01187](#)].
- [43] H. O. Silva, J. Sakstein, L. Gualtieri, T. P. Sotiriou and E. Berti, *Spontaneous scalarization of black holes and compact stars from a Gauss-Bonnet coupling*, *Phys. Rev. Lett.* **120** (2018) 131104, [[1711.02080](#)].
- [44] Y. S. Myung and D.-C. Zou, *Gregory-Laflamme instability of black hole in Einstein-scalar-Gauss-Bonnet theories*, *Phys. Rev. D* **98** (2018) 024030, [[1805.05023](#)].
- [45] B.-H. Lee, W. Lee and D. Ro, *Expanded evasion of the black hole no-hair theorem in dilatonic Einstein-Gauss-Bonnet theory*, *Phys. Rev. D* **99** (2019) 024002, [[1809.05653](#)].
- [46] B.-H. Lee, H. Lee and W. Lee, *Hairy black holes in dilatonic Einstein-Gauss-Bonnet theory*, in *17th Italian-Korean Symposium on Relativistic Astrophysics*, 11, 2021, [2111.13380](#).
- [47] A. Papageorgiou, C. Park and M. Park, *Rectifying no-hair theorems in Gauss-Bonnet theory*, *Phys. Rev. D* **106** (2022) 084024, [[2205.00907](#)].
- [48] Y.-H. Hyun, B. Latosh and M. Park, *Scalar Field Perturbation of Hairy Black Holes in EsGB theory*, [2405.08769](#).
- [49] B.-H. Lee, W. Lee and D. Ro, *Fubini instantons in Dilatonic Einstein–Gauss–Bonnet theory of gravitation*, *Phys. Lett. B* **762** (2016) 535–542, [[1607.01125](#)].
- [50] X. Y. Chew, G. Tumurtushaa and D.-h. Yeom, *Euclidean wormholes in Gauss–Bonnet-dilaton gravity*, *Phys. Dark Univ.* **32** (2021) 100811, [[2006.04344](#)].
- [51] B.-H. Lee, W. Lee, D.-h. Yeom and L. Yin, *Gravitational waves from the vacuum decay with LISA*, *Chin. Phys. C* **46** (2022) 075101, [[2106.07430](#)].
- [52] R. Nair, S. Perkins, H. O. Silva and N. Yunes, *Fundamental Physics Implications for Higher-Curvature Theories from Binary Black Hole Signals in the LIGO-Virgo Catalog GWTC-1*, *Phys. Rev. Lett.* **123** (2019) 191101, [[1905.00870](#)].
- [53] M. Okounkova, *Numerical relativity simulation of GW150914 in Einstein dilaton Gauss-Bonnet gravity*, *Phys. Rev. D* **102** (2020) 084046, [[2001.03571](#)].
- [54] H.-T. Wang, S.-P. Tang, P.-C. Li, M.-Z. Han and Y.-Z. Fan, *Tight constraints on Einstein-dilation-Gauss-Bonnet gravity from GW190412 and GW190814*, *Phys. Rev. D* **104** (2021) 024015.
- [55] S. E. Perkins, R. Nair, H. O. Silva and N. Yunes, *Improved gravitational-wave constraints on higher-order curvature theories of gravity*, *Phys. Rev. D* **104** (2021) 024060, [[2104.11189](#)].

- [56] Z. Lyu, N. Jiang and K. Yagi, *Constraints on Einstein-dilation-Gauss-Bonnet gravity from black hole-neutron star gravitational wave events*, *Phys. Rev. D* **105** (2022) 064001, [[2201.02543](#)].
- [57] P. Salati, *Quintessence and the relic density of neutralinos*, *Phys. Lett. B* **571** (2003) 121–131, [[astro-ph/0207396](#)].
- [58] F. Rosati, *Quintessential enhancement of dark matter abundance*, *Phys. Lett. B* **570** (2003) 5–10, [[hep-ph/0302159](#)].
- [59] J. U. Kang and G. Panotopoulos, *Big-Bang Nucleosynthesis and neutralino dark matter in modified gravity*, *Phys. Lett. B* **677** (2009) 6–11, [[0806.1493](#)].
- [60] S. Capozziello, M. De Laurentis and G. Lambiase, *Cosmic relic abundance and $f(R)$ gravity*, *Phys. Lett. B* **715** (2012) 1–8, [[1201.2071](#)].
- [61] S. Capozziello, V. Galluzzi, G. Lambiase and L. Pizza, *Cosmological evolution of thermal relic particles in $f(R)$ gravity*, *Phys. Rev. D* **92** (2015) 084006, [[1507.06835](#)].
- [62] M. T. Meehan and I. B. Whittingham, *Dark matter relic density in scalar-tensor gravity revisited*, *JCAP* **12** (2015) 011, [[1508.05174](#)].
- [63] G. Lambiase, *$f(R)$ cosmology and dark matter*, *PoS DSU2015* (2016) 012.
- [64] F. D’Eramo, N. Fernandez and S. Profumo, *When the Universe Expands Too Fast: Relentless Dark Matter*, *JCAP* **05** (2017) 012, [[1703.04793](#)].
- [65] W. Buchmuller, R. D. Peccei and T. Yanagida, *Leptogenesis as the origin of matter*, *Ann. Rev. Nucl. Part. Sci.* **55** (2005) 311–355, [[hep-ph/0502169](#)].
- [66] S. Kawai and J. Kim, *Gauss–Bonnet Chern–Simons gravitational wave leptogenesis*, *Phys. Lett. B* **789** (2019) 145–149, [[1702.07689](#)].
- [67] J. Ghiglieri and M. Laine, *Gravitational wave background from Standard Model physics: Qualitative features*, *JCAP* **07** (2015) 022, [[1504.02569](#)].
- [68] J. Ghiglieri, G. Jackson, M. Laine and Y. Zhu, *Gravitational wave background from Standard Model physics: Complete leading order*, *JHEP* **07** (2020) 092, [[2004.11392](#)].
- [69] A. Ito, T. Ikeda, K. Miuchi and J. Soda, *Probing GHz gravitational waves with graviton–magnon resonance*, *Eur. Phys. J. C* **80** (2020) 179, [[1903.04843](#)].
- [70] N. Herman, L. Lehoucq and A. Fúfza, *Electromagnetic antennas for the resonant detection of the stochastic gravitational wave background*, *Phys. Rev. D* **108** (2023) 124009, [[2203.15668](#)].
- [71] G. Steigman, B. Dasgupta and J. F. Beacom, *Precise Relic WIMP Abundance and its Impact on Searches for Dark Matter Annihilation*, *Phys. Rev. D* **86** (2012) 023506, [[1204.3622](#)].
- [72] E. W. Kolb and M. S. Turner, *The Early Universe*, vol. 69. Addison-Wesley Publishing Company, 1990, [10.1201/9780429492860](#).
- [73] PLANCK collaboration, N. Aghanim et al., *Planck 2018 results. VI. Cosmological parameters*, *Astron. Astrophys.* **641** (2020) A6, [[1807.06209](#)].
- [74] S. Tsujikawa, *Quintessence: A Review*, *Class. Quant. Grav.* **30** (2013) 214003, [[1304.1961](#)].
- [75] M. Cicoli, S. De Alwis, A. Maharana, F. Muia and F. Quevedo, *De Sitter vs Quintessence in String Theory*, *Fortsch. Phys.* **67** (2019) 1800079, [[1808.08967](#)].
- [76] Y. S. Myung, T. Moon and B.-H. Lee, *Revisiting slow-roll inflation in nonminimal derivative coupling with potentials*, *JCAP* **10** (2015) 007, [[1505.04027](#)].

- [77] S. D. Odintsov and V. K. Oikonomou, *Autonomous dynamical system approach for $f(R)$ gravity*, *Phys. Rev. D* **96** (2017) 104049, [[1711.02230](#)].
- [78] N. Chatzarakis and V. K. Oikonomou, *Autonomous dynamical system of Einstein–Gauss–Bonnet cosmologies*, *Annals Phys.* **419** (2020) 168216, [[1908.08141](#)].
- [79] E. A. Coddington and N. Levinson, *Theory of Ordinary Differential Equations*. McGraw-Hill, New Delhi, 1955.
- [80] E. Braaten and R. D. Pisarski, *Soft Amplitudes in Hot Gauge Theories: A General Analysis*, *Nucl. Phys. B* **337** (1990) 569–634.
- [81] A. Ringwald, J. Schütte-Engel and C. Tamarit, *Gravitational Waves as a Big Bang Thermometer*, *JCAP* **03** (2021) 054, [[2011.04731](#)].
- [82] M. Maggiore, *Gravitational Waves. Vol. 2: Astrophysics and Cosmology*. Oxford University Press, 3, 2018.
- [83] M. Kamionkowski, A. Kosowsky and M. S. Turner, *Gravitational radiation from first order phase transitions*, *Phys. Rev. D* **49** (1994) 2837–2851, [[astro-ph/9310044](#)].
- [84] S. J. Huber and T. Konstandin, *Gravitational Wave Production by Collisions: More Bubbles*, *JCAP* **09** (2008) 022, [[0806.1828](#)].
- [85] T.-H. Yeh, J. Shelton, K. A. Olive and B. D. Fields, *Probing physics beyond the standard model: limits from BBN and the CMB independently and combined*, *JCAP* **10** (2022) 046, [[2207.13133](#)].
- [86] L. Pagano, L. Salvati and A. Melchiorri, *New constraints on primordial gravitational waves from Planck 2015*, *Phys. Lett. B* **760** (2016) 823–825, [[1508.02393](#)].
- [87] T. C. C. et. al., *Core (cosmic origins explorer) a white paper*, 2011.
- [88] R. L. et. al., *Euclid definition study report*, 2011.
- [89] K. Kuroda, W.-T. Ni and W.-P. Pan, *Gravitational waves: Classification, Methods of detection, Sensitivities, and Sources*, *Int. J. Mod. Phys. D* **24** (2015) 1530031, [[1511.00231](#)].
- [90] F. Muia, F. Quevedo, A. Schachner and G. Villa, *Testing BSM Physics with Gravitational Waves*, [2303.01548](#).